The Pennsylvania State University

The Graduate School

DUST FEED AND WEAVE TOPOLOGY EFFECTS IN GAS TURBINE COOLING

A Thesis in

Mechanical Engineering

by

Trevor M. Cory

Submitted in Partial Fulfillment
of the Requirements
for the Degree of

Master of Science

December 2020

The thesis of Trevor M. Cory was reviewed and approved by the following:

Karen A. Thole
Department Head of Mechanical Engineering
Distinguished Professor
Thesis Advisor

Stephen P. Lynch
Professor of Mechanical Engineering

Daniel C. Haworth
Associate Department Head for Graduate Programs of Mechanical Engineering
Professor of Mechanical Engineering

ABSTRACT

As gas turbine temperatures continue increasing to improve performance and efficiency, understanding the mechanisms associated with cooling technologies is essential for preventing part failure and extending the life cycles of hot section components. One detriment to turbine cooling is the presence of dirt deposition. Particulates that enter the turbine section's coolant flow can impede cooling performance by blocking flow passages. On the improvement side, there is ongoing research in considering materials to reduce the amount of necessary cooling. Ceramic matrix composites (CMCs) are one such material of interest for gas turbine components because of their favorable weight and thermal properties. However, much like dirt depositing on surfaces, the unique surface topology of a CMC can have a significant impact on the convective heat transfer inherent to turbine cooling technologies.

The research of this thesis includes a study of dirt deposition in a double-walled cooling design that includes an impingement plate followed by an effusion plate, which is commonly used for combustor liners. In deposition testing, two different dirt feed mechanisms were used to introduce dirt into a coolant flow. The slug feed method consisted of dirt particles being introduced to the flow in discrete bursts known as slugs. The continuous feed method introduced dirt particles to the flow in a constant flow, which was developed to allow versatility in controlling dirt loading rates. Experiments were conducted with varying pressure ratios, amounts of dirt, and in heated and unheated conditions. Results showed that the slug feed method resulted in a higher capture efficiency and dirt accumulation on the inside of the effusion plate than did the continuous feed.

As a second part of this study, different CMC surface topologies were investigated. Three orientations of a weave pattern were additively manufactured as the walls of an internal channel. Bulk pressure losses and heat transfer coefficients were measured experimentally over a range of Reynolds numbers for each channel geometry. To gain further understanding of experimental results computational fluid dynamics (CFD) simulations were also conducted. Results showed that the introduction of a weave surface to one channel wall caused augmentations of friction factor and Nusselt number over a channel with smooth walls; friction factor augmentations being the higher of the two. The largest augmentations occurred when the weave strands were perpendicular to the flow direction. Introducing the weave surface to a second channel wall further increased augmentation values with the weave strands perpendicular to the flow consistently resulting in the highest augmentations.

TABLE OF CONTENTS

List of Figures vii

List of Tables xi

Nomenclature xii

ACKNOWLEDGEMENTS xiv

Chapter 1 Introduction 1

- 1.1 Dust Deposition in Gas Turbines 2
- 1.2 Ceramic Matrix Composites in Gas Turbines 2
- 1.3 Objectives and Document Outline 3

Chapter 2 Impact of Dust Feed on Capture Efficiency and Deposition Patterns in a Double-Walled Liner 3

- Abstract 3
- 2.1 Introduction 4
- 2.2 Literature Review 5
- 2.3 Double-Walled Cooling Geometry 7
- 2.4 Dirt Characterization and Test Conditions 9
- 2.5 Experimental Setup 12
  - 2.5.1 Dirt Pattern Characterization 14
  - 2.5.2 Experimental Uncertainty 17
- 2.6 Effect of Feed Type 18
- 2.7 Effect of Backflow Margin 23
- 2.8 Effect of Temperature 26
- 2.9 Conclusions 31

Chapter 3 Impact of Ceramic Matrix Composite Topology on Friction Factor and Heat Transfer 33

- Abstract 33
- 3.1 Introduction 34
- 3.2 Literature Review 35
- 3.3 Weave Pattern Geometry and Manufacturing 36
- 3.4 Experimental Setup and Methodology 43
  - 3.4.1 Experimental Uncertainty 45
- 3.5 Computational Fluid Dynamics Setup 45
- 3.6 Impact of Hydraulic Diameter Calculation 47

3.7 Weave Orientation Effects for One Wall Coupons..49
3.8 Weave Alignment Effects for Two Wall Coupons 57
3.9 Conclusions...63

Chapter 4 Conclusions and Recommendations..65

4.1 Recommendations for Future Work..67

References..68

LIST OF FIGURES

Figure 2.1. Double-walled cooling geometry. On the left, the impingement plate hole geometry with solid black lines overlays the effusion plate hole geometry with dotted black lines. The area of interest when measuring dirt thickness is inside the red square. Flow goes into the page. The right shows a simple cross section model of the double-walled cooling geometry. 8

Figure 2.2. Particle size distribution of AFRL-05 [29]. 10

Figure 2.3. Slug feed mechanism. Initially, bottom ball valve is closed while dirt is fed into launch chamber. The chamber was then pressurized, the top ball valve was closed, then the bottom valve opened to introduce dirt into mainstream. Double-walled cooling geometries are mounted to the double-pass heat exchanger. 13

Figure 2.4: Continuous feed mechanism. Dirt is laid onto the plate, then blown off through the use of a jet of air through the capillary tube. The capillary tube is driven by a stepper motor, and traverses the entire length of the plate throughout a test, from left to right. 14

Figure 2.5. Scan process of the post-test effusion plate. The effusion plate is first scanned, and then an in-house code is used to process the generated point cloud. The point cloud is flattened, overlaid with the matching effusion plate CAD model, and then dirt thickness is calculated by subtracting the clean scan height from the dirty scan height. 16

Figure 2.6. Average capture efficiencies for each of the two different feed mechanisms with uncertainty bars at two points. Experiments were conducted at room temperature at a BFM of 3.42%. 19

Figure 2.7. Average capture efficiency and dirt thicknesses over all directly comparable tests between the slug and continuous feed mechanisms. Experiments were conducted at room temperature. 20

Figure 2.8. Laterally averaged dirt thickness traces along the effusion plate when 105 mg of dirt is introduced. Experiments were conducted at room temperature and at BFM of 3.42%. 22

Figure 2.9. Post-test microscope pictures depicting dirt accumulation patterns on the effusion plate ‘s upstream face. Dirt accumulation corresponds with the light-colored surfaces. Pictures A and B show slug and continuous feed tests, respectfully, with 105 mg of dirt introduced. Pictures C and D show slug and continuous feed tests, respectfully, with 420 mg of dirt introduced. Experiments were completed at room temperature and at a BFM of 3.42%. 22

Figure 2.10. Average capture efficiencies for each of the two different feed mechanisms with uncertainty bars at two points. Experiments were conducted at room temperature with 420 mg of dirt introduced. 24

Figure 2.11. Post-test microscope pictures depicting dirt accumulation patterns on the effusion plate ‘s upstream face. Dirt accumulation corresponds with the light-colored surfaces. Pictures A and B show slug and continuous feed tests, respectfully, at a BFM of 1.33%. Pictures C and D show slug and continuous feed tests, respectfully, at a BFM of 4.32%. Experiments were completed at room temperature and with 420 mg of dirt introduced....24

Figure 2.12. Laterally averaged dirt thickness traces along the effusion plate. Experiments were conducted at room temperature, at a BFM of 1.33%, and with 420 mg of dirt introduced....25

Figure 2.13. Laterally averaged dirt thickness traces along the effusion plate. Experiments were conducted at room temperature, at a BFM of 4.32%, and with 420 mg of dirt introduced....26

Figure 2.14. Capture efficiency and average dirt thickness for both heated and unheated conditions. Experiments were conducted with the continuous feed mechanism, at a BFM of 4.32%, and with 420 mg of dirt introduced....27

Figure 2.15. Post-test microscope pictures depicting dirt accumulation patterns on the effusion plate ‘s upstream face. Dirt accumulation corresponds with the light-colored surfaces. Pictures A and B show unheated and heated tests, respectfully, at a BFM of 2.08%. Pictures C and D show unheated and heated tests, respectfully, at a BFM of 4.32%. Experiments were completed with 420 mg of dirt introduced....29

Figure 2.16. Laterally averaged dirt thickness traces. Experiments were conducted with continuous feed, a BFM of 4.32%, and 420 mg of dirt introduced....29

Figure 2.17. Average capture efficiencies at a variable BFM with uncertainty bars at two points. Experiments were conducted with continuous feed and 420 mg of dirt introduced....30

Figure 2.18. Average dirt thickness at a variable BFM with uncertainty bars at two points. Experiments were conducted with continuous feed and 420 mg of dirt introduced....30

Figure 3.1. (1a) shows the coupon model with design channel dimensions. (1b) shows a cross section view of the bottom channel wall with a weave surface created by six adjacent weave RUCs. (1c) and (1d) show a top down view and side cross section view of the RUC....38

Figure 3.2. Top-down view of the bottom channel walls for the three different weave orientation angles....40

Figure 3.3. Top-down view of the 0° weave channel walls for the aligned case (top) and for the staggered weave pattern....40

Figure 3.4. Different methods for calculating D_h using (4a) Method 1 with cross sectional slices of the channel and (4b) Method 2 with a fixed rectangular shape....42

Figure 3.5. D_h of each coupon geometry using calculation methods 1 and 2....43

Figure 3.6. Schematic of experimental rig used for pressure drop and heat transfer experiments. 44

Figure 3.7. (7a) shows an example of the entire simulation meshes. (7b) shows views of the mesh at the center plane of the models. 46

Figure 3.8. Friction factor over a range of Reynolds numbers for the 0° coupons using Dh calculation methods 1 and 2. 48

Figure 3.9. Nusselt number over a range of Reynolds numbers of the 0° coupons using Dh calculation methods 1 and 2. 49

Figure 3.10. Friction factor for a range of Reynolds numbers for the coupons containing one weave wall. 50

Figure 3.11. Friction factor augmentation for a range of Reynolds numbers of the coupons containing one weave wall. 51

Figure 3.12. Nusselt number for a range of Reynolds numbers of the coupons containing one weave wall. 52

Figure 3.13. Nusselt number augmentation for a range of Reynolds numbers of the coupons containing one weave wall. 53

Figure 3.14. Top-down view of local Nusselt number contours for Re = 40,000 on the full length of the one weave wall coupons for the (14a) 0° orientation, (14b) 45° orientation, and (14c) 90° orientation. 54

Figure 3.15. Cross-sectional view of normalized temperature at Re = 40,000 at an x/L distance of 0.9 for the (15a) 0° orientation, (15b) 45° orientation, and (15c) 90° orientation. 55

Figure 3.16. Normalized temperature fields at Re = 40,000 in the fully developed region of 0.67 < x/L < 0.83 including expanded views for the (16a) 0° orientation, (16b) 45° orientation, and (16c) 90° orientation. 56

Figure 3.17. Friction factor augmentation over a range of Reynolds numbers of the 0° and 90° coupons containing one and two weave walls. 57

Figure 3.18. Normalized temperature contours with velocity vectors at the centerline of the channels between x/L of 0 and 0.1 with Re = 40,000. Figure (18a) shows the 90-2W-A coupon and (18b) shows the 90-2W-S coupon. 60

Figure 3.19. Nusselt number augmentation over a range of Reynolds numbers of the 0° and 90° coupons containing one and two weave walls. 61

Figure 3.20. Nusselt number and friction factor augmentations of all weave geometries compared to additively manufactured microchannels from Stimpson et al. [50] and ribbed channels from Park et al. [56]. Aspect ratios of the weave channels are all 5.

Aspect ratios of the ribbed channels are 2 and 4. Aspect ratios 2.3 and 2.1 of the microchannels are named L-1x-In and M-2x-In, respectively, in Stimpson et al. [50]. ..62

LIST OF TABLES

Table 2.1: Dimensions of the Impingement and Effusion Plates 8

Table 2.2: Dirt Flow Characteristics 11

Table 2.3: Heated and Unheated Test Matrices 11

Table 3.1. RUC Dimensions 38

Table 3.2. Coupon Geometry Types 39

NOMENCLATURE

BFM	Back flow margin
CAD	Computer aided design
d	particle diameter
D	impingement and effusion hole diameter
P_{down}	pressure downstream of effusion plate
P_{up}	total pressure upstream of impingement plate
Re_{jet}	jet Reynolds number, $\rho \cdot U_{jet} \cdot D \cdot \mu^{-1}$
Re_p	particle Reynolds number, $\rho \cdot U_{jet} \cdot d \cdot \mu^{-1}$
St	effective Stokes number, $\psi \cdot \frac{\rho_d \cdot d^2 \cdot U_{jet}}{18 \cdot \mu \cdot D}$
U_{jet}	impingement jet velocity
D_{tot}	total mass of dirt intended for introduction
D_{imp}	mass of dirt on outside of impingement plate
D_{int}	actual mass of dirt introduction; $D_{int} = D_{tot} - D_{imp}$
M_{eff}	mass of effusion plate post-test
M_{cl}	mass of effusion plate post-cleaning
h_{avg}	average dirt thickness
h_L	laterally averaged dirt thickness
RUC	repeating unit cell
H	channel height
W	channel width
L_{RUC}	repeating unit cell length
w_t	tow width
s_t	tow pitch
h_f	fabric height
h_w	weave peak
RMS_w	root-mean square roughness of the weave
M	number of surface data points
z_{surf}	actual RUC surface height
z_{des}	design intent RUC surface height

D_h	hydraulic diameter
N	number of slices
A_c	channel cross-sectional area
P	channel perimeter
Re	Reynolds number, $\frac{uD_h}{\nu}$
u	mass averaged velocity
K_s	sandgrain roughness
f	friction factor, $\frac{2D_h}{L}\frac{\Delta P}{\rho v^2}$
h	convective heat transfer coefficient, $\frac{Q_{flow}}{A_s \Delta T_{LM}}$
Nu	Nusselt number, $\frac{hD_h}{k}$
Pr	Prandlt number
T	flow temperature
T_{in}	inlet flow temperature
T_s	channel surface temperature
p	rib spacing
e	rib height
AR	channel aspect ratio

Greek

ρ	flow density
ρ_d	dirt particle density
μ	dynamic viscosity
η_c	capture efficiency
ψ	drag correction coefficient [1]
ν	kinematic viscosity
θ	normalized temperature, $\frac{T-T_{in}}{T_s-T_{in}}$

Subscripts

0	reference condition

ACKNOWLEDGEMENTS

First, I would like to thank my advisor, Dr. Karen Thole, for providing me the opportunity to work in the Penn State START Lab. Her mentorship throughout my graduate school career has continually pushed me to put forth the best work that I possibly can. Additionally, I would like to thank Dr. Stephen Lynch whose technical advice was always appreciated.

I would also like to thank Pratt & Whitney, without which, my research would not have been possible. Specifically, Ryan Lundgreen, Robin Prenter, Stephen Kramer, Tyler Vincent, and San Quach proved to be invaluable industry sponsors with their technical expertise.

Last but not least, I'd like to thank my friends and family who have been so supportive throughout this process. To my lab-mates, it has been a pleasure working with all of you. The comradery and willingness to help each other was entertaining, inspirational, and a blessing. To my friends from afar, thank you for making the highs even higher and softening the lows. To Mackenzie Woodard, thank you for always supporting me, making my life interesting, and taking care of me. And to my family, thank you for being a solid foundation through my time here. I share my achievements with you.

Chapter 1

Introduction

The gas turbine is largely used for industrial power generation or propulsion in aerospace applications. The first stage of a gas turbine consists of a compressor which increases the pressure and temperature of the incoming air. The pressurized air then enters the combustor or is bled off from the main gas path to be used as coolant flow. In the combustor, air is mixed with fuel and ignited, dramatically increasing in temperature and enthalpy. Gas from the combustor then travels through the turbine where it expands and passes through blades that extract the gas's enthalpy, converting it into work. Part of this work is then used to power the compressor and the remaining work is used to power an electric generator or propel an aircraft in power generation and aerospace applications, respectively.

With main gas path temperatures in the combustor and turbine reaching above the melting points of engine components, effectively cooling those components is imperative for extending part life. Internal cooling passages are used to convectively extract heat from engine components and then the coolant can be expelled from these components to create a protective layer of cooler gas over the external part surfaces. Since the cooling flow is bled from the high pressure compressor and does not generate work for the engine, keeping the amount of cooling flow to a low level for increased efficiency while also providing engine components the necessary amount of cooling to remain functional is a significant challenge. Therefore, extensive research is conducted on gas turbine cooling technologies to protect engine parts and improve overall efficiency. The research discussed in this thesis will cover two notable topics in turbine cooling: dirt deposition in a double-walled cooling scheme and the effects of ceramic matrix composite (CMC) weave surfaces in internal flow.

1.1 Dirt Deposition in Gas Turbines

Particle ingestion is a growing issue in gas turbines, especially relevant to flights over developing countries or in areas with poor air quality. When a gas turbine intakes particles, these particles can be compressed and enter the cooling passages bled from the compressor. The particles can then deposit within cooling passages and around effusion holes that are important for keeping hot section parts from failing. Once deposited, the particles can insulate parts from receiving the cooling they need as well as block cooling flow. The goal of deposition research is to better understand the driving mechanisms causing deposition so that their effects can be reduced or prevented in new gas turbine designs.

1.2 Ceramic Matrix Composites in Gas Turbines

CMCs are a growing material of interest in gas turbines due to their favorable weight and thermal properties. These materials consist of ceramic fibers embedded within a ceramic matrix. Much like traditional ceramics that are often used in temperature or environmental barrier coatings for current hot section components, CMCs retain the ability to withstand high temperatures. This capability provides a crucial advantage for CMCs over nickel-based super alloys used in current gas turbine components. Resulting from the structure of woven fibers, CMCs also boast increased toughness compared to traditional ceramics, allowing them to be considered for the harsh environments of the gas turbine hot sections. The vast majority of current CMC research has investigated this material’s development and structural properties so as to understand where this material can be safely implemented in gas turbines. However, the effects of the inherent woven surface of a CMC on convective heat transfer has not been investigated in the majority of public CMC studies.

1.3 Objectives and Document Outline

This thesis reports the effects of dirt deposition within a double-walled cooling scheme relevant to a combustor liner. Another study of interest was investigating the effect of a surface morphology relevant to a CMC in the form of a weave pattern for a channel flow. Chapter 2 covers deposition testing and is composed of a paper published in the ASME Turbo Expo 2019 conference. Deposition results will include capture efficiency and dirt thickness measurements as well as microscope pictures of deposition patterns. Chapter 3 will cover weave surface testing which has been submitted for Turbo Expo 2021 and the *Journal of Turbomachinery*. Weave surface results will include friction factor, Nusselt number, and supporting CFD evidence. Chapter 4 will summarize the major findings of these two studies and provide recommendations for future work. The overall objective of this thesis is to provide valuable contributions to gas turbine cooling research in the specific fields of deposition and CMC relevant cooling passages.

Chapter 2

Impact of Dust Feed on Capture Efficiency and Deposition Patterns in a Double-Walled Liner[1]

Abstract

The introduction of particulates into gas turbine engines poses a serious threat to component durability. Particles drawn from the environment, such as ash or sand, can be introduced into the air system used to cool hot section components and drastically diminish cooling

[1] Cory T. M., Thole, K. A., Kirsch K. L., Lundgreen R., Prenter R., and Kramer S., 2019, “Impact of Dust Feed on Capture Efficiency and Deposition Patterns in a Double-Walled Liner,” Proc. ASME Turbo Expo, GT2019-90981.

performance. In the current study, a dirt-laden coolant stream impinged on a double-walled cooling configuration, which was comprised of an impingement plate followed by an effusion-cooled plate. Experiments were conducted at both room temperature and at temperatures in excess of 750°C; flow conditions were varied to achieve different pressure ratios across the cooling configuration. Dirt particles were introduced into the coolant using two different methods: in discrete bursts, called slugs; or in a continuous feed ensuring a constant stream of particles. This continuous feed mechanism is at the crux of a new test facility created to introduce flexibility and precision in the control of dirt feed rates, particularly for very small (<50 mg) amounts of dirt.

The difference in capture efficiency and in dirt patterns between the two feed methods showed measurably different dirt accumulation levels on the cold side of the effusion plate at the same test conditions. Results show that the slug feed method caused higher capture efficiency and thicker dirt deposition on the effusion plate compared to the continuous feed.

2.1 Introduction

As global flight patterns increasingly traverse across developing nations, the threat of particle ingestion in aircraft engines grows. Poor air quality affects the performance of aircraft engines differently depending on the location in the engine. In the cold section, erosion is the concern: environmental particulates drawn in by the fan can subsequently erode compressor blades. In the hot section, deposition on and within components greatly reduces their durability.

Both the fan and compressor sections work to pulverize the particulates. Once reaching the high pressure compressor section, from where air is bled to cool hot section components, the particles are small enough to be easily taken by secondary cooling systems. Any particles not taken by the secondary cooling flow pose a threat for deposition and can negatively affect external cooling features, such as film cooling. Particles taken by the cooling flow, on the other hand, jeopardize internal cooling performance. Once in the elevated temperatures of the hot section, the particles more readily stick within internal cooling systems. The result can be unwanted insulation on the internal walls or channels that become blocked altogether. Where and how the dirt particles deposit within a hot section component strongly depend on their size, temperature, the internal cooling geometry, and the introduction method. In the current study, AFRL, Air Force Research Laboratory, dirt was used, which had a nominal particle diameter of 1 μm. Experiments were conducted both at room temperature and at elevated temperatures, for which the adhesion forces were primarily in the form of Van der Waals forces [2][1]; the cooling scheme chosen for the study was a combined impingement and effusion cooling pattern. Two dirt introduction methods were employed, namely as a burst, known as a slug, and as a slow, continuous feed. The difference in dirt patterns between the two methods is the focus of this research.

2.2 Literature Review

Particles ingested by the hot section of gas turbine engines can be categorized broadly into two groups, namely particulates from alternative fuels and particulates from the environment, such as ash [3] or sand [4]. The damaging effects of these ingested particulates are well-documented [5]; both erosion and deposition pose serious threats to engine performance [6,7]. Moreover, issues derived from environmental particle ingestion will only grow as aircraft are increasingly deployed in areas with high volumes of atmospheric particulates [8]. Understanding how these particulates degrade performance, as well as developing models that predict the impacts of particulate ingestion, have been, and continue to be, the focus of many studies.

Whitaker et al. [9] studied, among other topics, the effects of particle size on blockage in a double-walled impingement cavity; the authors found that particles under 3.25 μm were primarily responsible for the blockage development for their particular internal cooling setup. Temperature, also, plays a key role in particle deposition: Crosby et al. [10] showed that deposition rates increased exponentially with increasing gas temperature, with deposition initiating at 960°C. Through an analysis of several deposition models [11–13], Hsu et al. [14] confirmed that both the particle and surface temperatures are key variables in predicting particle stickiness. Furthermore, as more particles stick to a surface, that surface's temperature increases due to insulation [15].

Numerous studies have investigated the effects of particle deposition on gas turbine cooling configurations, most notably the impacts on film cooling performance [16–21]. Ogiriki et al. [22] calculated that the creep life of a high pressure turbine blade can be reduced by as much as 79% if film cooling holes are blocked. Film blockage, however, is not the only adverse effect from deposition; increased surface roughness caused by deposited particles can lower film effectiveness because of the thicker boundary layer promoted by the rough features [23,24]. Additionally, the deposited particles provide insulation: Mensch and Thole [25] experimentally simulated molten particle deposition by injecting molten wax on a conducting blade endwall, which was cooled using both film and impingement holes. The presence of the wax degraded the combined film and impingement performance by 36% due to its insulating effect on the endwall.

Dunn et al. [26] found that particles ingested by gas turbines for aircraft propulsion are pulverized in the fan and compressor sections, and have an average size of 6 μm at the compressor exit. Such small particles can easily be taken through the internal air system, and can limit the performance of cooling schemes such as ribs [27], film holes [28], and impingement cooling [1,29]. Walsh et al. [26] used a dirt-laden coolant stream to investigate dirt patterns on the cold side of a film-cooled test plate; Cardwell et al. [27] furthered the study by investigating double-walled cooling patterns. Four geometric variations of test plate duos were studied, where the amount of overlap between impingement holes and film cooling holes was tested. The authors found that the test condition in which the impingement and film holes overlapped the most resulted in the highest flow blockage.

In laboratory experiments, the method by which particles are introduced to cooling schemes can influence the particle sticking behavior [28]; capturing engine-relevant dirt conditions is a challenge, especially if those conditions change depending on where the engine operates. In the current study, two very different dirt feed mechanisms were used to investigate dirt patterns and capture efficiency in a double-walled cooling configuration. The first feed mechanism introduced dirt to the test rig in discrete bursts, while the second mechanism introduced the dirt slowly and continuously. The second feed mechanism is the product of a brand new test facility, capable of introducing very small (<50 mg) amounts of dirt continuously over a prescribed period of time (>5 min). This study is unique in that it showcases the differences between these two feed mechanisms through detailed discussions on the amounts of dirt introduced, effects of temperature, and effects of pressure ratio.

2.3 Double-Walled Cooling Geometry

A double-walled cooling configuration was used to conduct experiments in the current study. In this arrangement, an impingement plate with straight holes resided upstream of an effusion plate with angled holes. Between the two lay a spacer plate of 2.5 hole diameters. The right side of Figure 2.1 shows a simple cross section model of the cooling geometry layout and direction of flow. The impingement and effusion holes do not directly overlap as shown in the left side of Figure 2.1, allowing the mainstream coolant flow to impact the face of the effusion plate once passing through the impingement holes. The area of interest, shown as the red square, marks the section of the effusion plate at which dirt thicknesses were measured. The boundaries of the test coupon plates interfered with the capture of dirt outside of this area of interest, deeming the outside region unnecessary in the scope of this study.

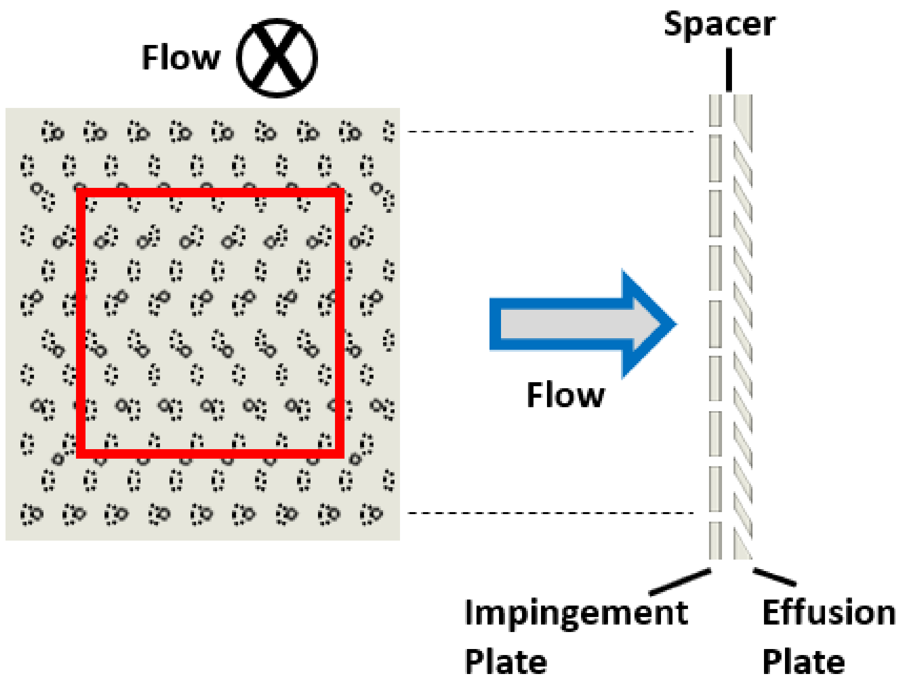

Figure 2.1. Double-walled cooling geometry. On the left, the impingement plate hole geometry with solid black lines overlays the effusion plate hole geometry with dotted black lines. The area of interest when measuring dirt thickness is inside the red square. Flow goes into the page. The right shows a simple cross section model of the double-walled cooling geometry.

As given in Table 1, the impingement plate included 8 rows of straight holes with spanwise spacings of 5.72 and 4.44 hole diameters. The effusion plate contained 12 rows of angled holes of the same diameter with spanwise spacings of 3.64 and 2.2 hole diameters.

Table 2.1. Dimensions of the Impingement and Effusion Plates

Plate	Number of Rows	Orientation

Impingement	8	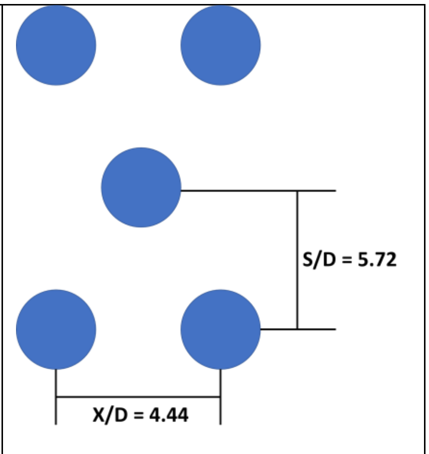
Effusion	12	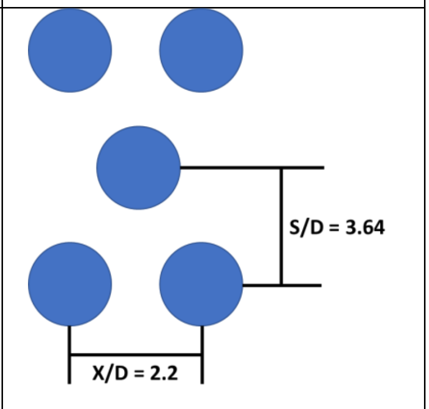

2.4 Dirt Characterization and Test Conditions

The dirt used for all experiments was AFRL 05, comprised primarily of quartz and gypsum. Density was quoted to be 2200 kg/m^3, with a particle diameter nominal size of 0 to 3 μm. Figure 2.2 details the particle size distribution of the dirt. The AFRL 05 had a high propensity to clump, forming larger, pebble-like masses. Before each test, the dirt was baked in order to reduce any effects of humidity on the results. The dirt was then sifted using a coarse mesh of arbitrary size. An effective Stokes number (St) was calculated for the dirt particles, assuming an average particle diameter of 1.2 μm. The particle Reynolds number (Re_p), calculated using the particle diameter and velocity through the impingement holes, ranged between 0.8 and 6 for all experiments; a drag correction factor, therefore, was applied to the calculations for the Stokes number. For St $\ll$1, the dirt particles are assumed to follow the flow path perfectly; for St $\gg$1, the dirt particles are assumed to be unaffected by the flow and exhibit more of a ballistic behavior.

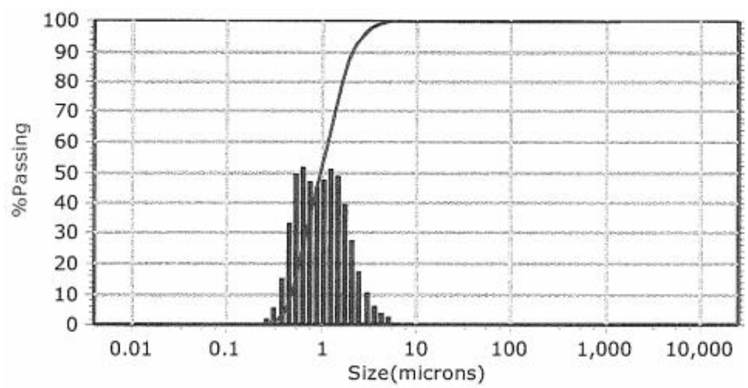

Figure 2.2. Particle size distribution of AFRL-05 [29].

Each of the continuous and slug feed mechanism tests were run at a variety of back flow margins (BFM), defined in Equation 2.1, which resulted in slightly different values for St.

$$\left[\frac{P_{up} + P_{down}}{P_{down}} \text{-}1\right] \cdot 100 = \text{BFM} \tag{2.1}$$

At a BFM of 1.3%, the lowest BFM tested, the effective Stokes number was calculated to be near 0.6 for both heated and unheated tests. At a higher BFM of 4.3%, Stokes number neared 1. The flow characteristics for the dirt at two different BFMs and two different rig temperatures are given in Table 2.2.

Table 2.2. Dirt Flow Characteristics

Rig Temp (°C)	BFM (%)	St	Re_p	Re_{jet}	Ma
25	4.3	1.0	6.4	3450	0.2
800	4.3	0.9	1.4	770	0.2
25	1.3	0.6	3.6	1950	0.1
800	1.3	0.5	0.8	430	0.1

In the current study, experiments were conducted to compare dirt deposition in slug and continuous feed mechanisms. In order to do so, experiments of varying dirt introduction amounts and varying BFMs were completed for both the slug and continuous feed mechanisms at room temperature, referred to as unheated conditions. In addition to the comparison of feed type, the effects of heated and unheated conditions were evaluated. Temperature sensitivity tests were conducted with varying dirt introduction amounts and varying BFMs using the continuous feed mechanism. Table 2.3 displays the various test conditions.

Table 2.3. Heated and Unheated Test Matrices

Heated Tests		
Feed Type	**Variable Dirt Amount [mg]**	**Variable BFM [%]**

	1.33 % BFM	420 mg Dirt
Continuous Feed	105	1.33
	420	2.08
	1260	2.82
	-	4.32
Unheated Tests		
Feed Type	**Variable Dirt Amount [mg] 3.42 % BFM**	**Variable BFM [%] 420 mg Dirt**
Slug	105	1.33
	420	2.82
	840	4.32
	1260	-
Continuous	105	1.33
	210	2.08
	420	2.82
	630	4.32
	1260	-
	2520	-

2.5 Experimental Setup

Experiments for the current study were conducted using air as the working fluid, which flowed through a double pass heat exchanger before reaching the impingement and effusion plates. The impingement and effusion plates were bolted to a mounting plate on the end of the heat exchanger, normal to a mainstream flow along the centerline of the heat exchanger, as seen in Figure 2.3. The mainstream flow exited to atmosphere. A thermocouple was placed along the centerline of the heat exchanger with a small metal cone around it. This baffle cone was implemented in order to disperse the dirt within the mainstream flow. The baffle cone was placed about 29.9D from the opening of the mainstream flow plenum of the heat exchanger and about 140D from the test section.

In the slug method of dirt introduction, dirt was divided into seven small piles of equal mass, referred to as slugs. Each slug was sequentially fed into a vertical pipe, perpendicular to mainstream flow and about 559D upstream of the heat exchanger; the manner in which the slugs were introduced is shown in Figure 2.3. A closed ball valve separated the dirt launch chamber and the mainstream flow. The chamber was then slightly pressurized, and the ball valve was released, shooting the dirt slug into the mainstream flow almost instantaneously. This pressurization of the chamber could possibly have a slight compaction effect on dirt, as discussed later in this study.

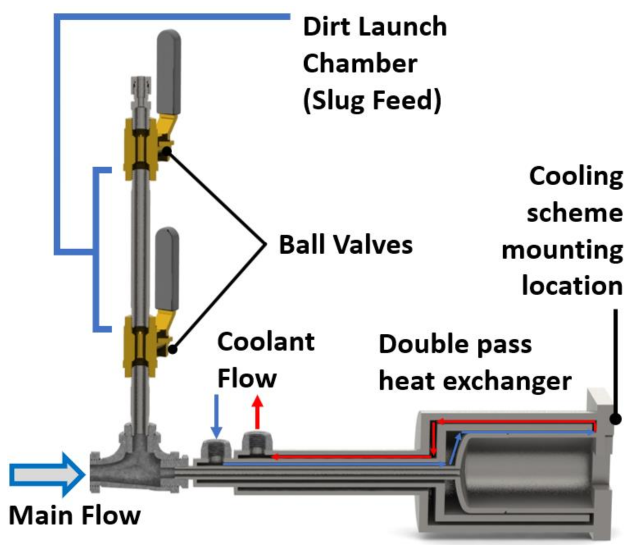

Figure 2.3. Slug feed mechanism. Initially, bottom ball valve is closed while dirt is fed into launch chamber. The chamber was then pressurized, the top ball valve was closed, then the bottom valve opened to introduce dirt into mainstream. Double-walled cooling geometries are mounted to the double-pass heat exchanger.

For the constant dirt feed methods, a new device was developed as shown in Figure 2.4. This device included a dirt plate, which was a narrow zinc-coated plate, where the dirt was evenly spread. The dirt plate was placed inside a larger diameter pipe. A capillary tube injected air aimed down toward the dirt plate and perpendicular to the mainstream flow. During a given test, the capillary tube traversed the length the plate using a pulley system controlled by a stepper motor. The dirt was blown off the plate and introduced into the crossflow, which was the cooling flow provided to the test coupons. The dirt loading rate was kept constant by adjusting the speed and duration of the stepper motor pulley system.

In each test, the percent back flow margin (BFM) was maintained at a constant value for the duration of the test. Static pressure in the test rig was measured upstream of the double pass heat exchanger. Given the dirt clogged the holes, the flowrate of the coolant was adjusted to maintain a constant back flow margin. During the heated tests, the effusion plate temperature and mainstream flow temperature were controlled independently by varying the coolant flow through a double-pass heat exchanger, which were all placed inside a kiln.

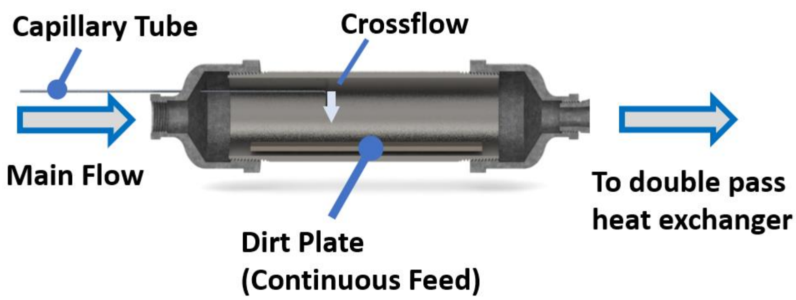

Figure 2.4: Continuous feed mechanism. Dirt is laid onto the plate, then blown off through the use of a jet of air through the capillary tube. The capillary tube is driven by a stepper motor, and traverses the entire length of the plate throughout a test, from left to right.

2.5.1 Dirt Pattern Characterization

Measurements of impingement and effusion plate masses were taken before and after each test. A third measurement of the effusion plate mass was taken after each test and after cleaning dirt off the plate. Dirt accumulation was determined by calculating the difference between the post-test "dirty" effusion plate mass (M_{eff}) and the post-test, post-cleaning effusion plate mass (M_{cl}) to account for any mass change due to oxidation. These measurements were used in the reported capture efficiency. Capture efficiency was calculated using Equation 2.2, and removed any dirt that did not reach the effusion plate. The D_{int} term in Equation 2.2 represented the total dirt introduced to the system minus the dirt on the cold side, or the side facing the mainstream flow, of the impingement plate. Additionally, any dirt that was found in the test section after each test was scraped out and weighed; that value was subtracted from the total dirt mass.

$$\frac{M_{eff} - M_{cl}}{D_{int}} \cdot 100 = \eta_c \tag{2.2}$$

After each experiment, the effusion plate geometries with dirt deposition were analyzed in two ways. First, photographs of the dirt patterns were taken using a laboratory microscope. Due to the viewing window, multiple pictures were necessary for each plate, which were then stitched together. These pictures allowed for qualitative analysis of the dirt patterns, which varied depending on experimental conditions.

The second analysis method was quantitative. Figure 2.5 shows the progression from raw scan data to quantified dirt thickness. A laser scanning device was used to take 3D scans of the dirt-covered effusion plate. The scan accuracy was 100 µm, and a scan resolution of 500 DPI was used to capture the dirt patterns [33]. A mount was created for the effusion plate and attached to scanner to ensure that each effusion plate was scanned at the same distance. After completing the scan, the plate's surface was then cleaned of any dirt and re-scanned. This process was completed while the plate was mounted to the scanner, allowing the plate to maintain its location in the scans' coordinate systems.

Once scanned, an in-house code was used to analyze the data. The plate scans were first flattened to eliminate any noise in the dirt thickness measurements resulting from any curves in the plate; the dirt thicknesses were uncompromised. Then the clean plate scan was overlaid with its corresponding CAD ensuring that the coordinate system of the scan matched that of the CAD model. Scans from all tests, therefore, were registered to a consistent coordinate system, resulting in a more straightforward comparison among tests. Dirt thickness was measured by subtracting the height of the dirty plate scan from that of the clean plate scan. By using this differential method to calculate dirt thickness, subtracting the two plate scans, any inherent bias from the scanner was produced in both scans and cancelled out. The dirt pattern in its entirety is shown in the final scan contour plot of Figure 2.5; however, to discount any edge effects, a region of interest was created that focused only on the center of the impingement holes. Afterward, a laterally averaged dirt thickness trace in the region of interest was plotted to compare dirt peak heights and shapes between tests. Plots showing laterally averaged traces are not to be confused with actual traces of dirt peaks. Regions of little to no deposition averaged with regions of deposition peaks result in laterally averaged traces that show "peaks" which are shorter than the actual dirt peak heights.

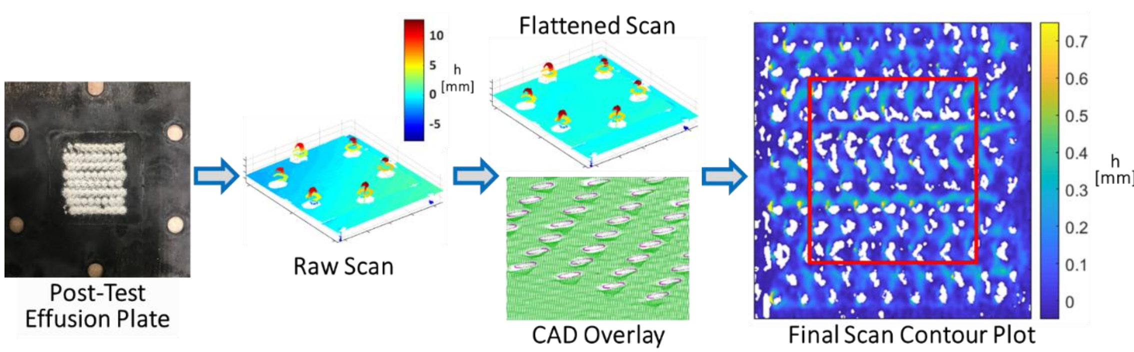

Figure 2.5. Scan process of the post-test effusion plate. The effusion plate is first scanned, and then an in-house code is used to process the generated point cloud. The point cloud is flattened, overlaid with the matching effusion plate CAD model, and then dirt thickness is calculated by subtracting the clean scan height from the dirty scan height.

2.5.2 Experimental Uncertainty

Uncertainty in the experimental methods was quantified using the methods proposed in Kline and McClintock [34]. The uncertainty in the BFM calculation was determined to be under 1% for all tests, regardless of the temperature at which the experiment was run. Specifically, an uncertainty of less than 1% for a BFM of 3.42% was calculated to be less than +/- 0.0342. The uncertainty in the mass flowrate measurement was also quite low and was calculated to be under 0.5%.

Uncertainties from the 3D scanner were determined by first repeating scan measurements of a basic plate geometry and calculating the 95% confidence interval. The repeatability uncertainty of the scanner was then combined with the 95% confidence interval of the experimental data repeatability for an overall dirt thickness measurement uncertainty. Bias uncertainty was removed from plate scans because of the differential method in measuring dirt thickness. In unheated test conditions, total uncertainty was found to be +/- 0.012 mm. Heated test conditions produced a total uncertainty of +/- 0.055 mm.

Another source of experimental uncertainty came in the calculation of the capture efficiency. A high resolution laboratory scale was used to measure the mass of the effusion plates before and after each test; the uncertainty in those weight measurements was 0.06%. However, the repeatability in capture efficiency among tests of the same experimental conditions was ±10% for slug tests and ±7% for continuous feed tests. All tests were repeated two to three times. As was seen in Figure 2.3, the flow path traversed by the dirt included two ball valves, onto which dirt readily stuck, and a 90° bend. The inability to quantify the amount of dirt that remained on the ball valves, as well as in all piping, was the largest source of repeatability error in the capture efficiency for slug tests. For continuous feed tests, the repeatability was improved over the slug tests because of the lack of ball valves; the flow path for the dirt was straight, which can be observed in Figure

2.4. Additionally, quantifying the amount of dirt that remained in the test facility after the continuous feed tests was more straightforward and feasible.

2.6 Effect of Feed Type

Two methods of dirt introduction were compared in unheated test conditions at room temperature. Figure 2.6 shows that on average, the slug feed resulted in significantly higher capture efficiency of dirt by the effusion plate at a BFM of 3.42%. Additionally, the trends between the two feed mechanisms differed: for the slug tests, the capture efficiency decreased as the amount of dirt introduced into the rig increased. For the continuous feed tests, however, the capture efficiency remained nearly constant. This trend suggests that the slug feed mechanism is more sensitive to the amount of dirt introduced.

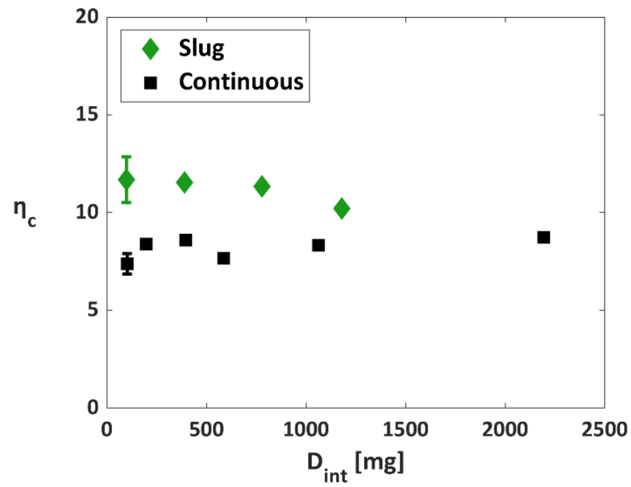

Figure 2.6. Average capture efficiencies for each of the two different feed mechanisms with uncertainty bars at two points. Experiments were conducted at room temperature at a BFM of 3.42%.

As previously mentioned, in each slug test, seven dirt doses of equal dirt mass, totaling to equal the dirt mass of the continuous feed, were introduced into the rig. Tests with more dirt introduced, therefore, meant that each dose contained a higher mass of dirt. One hypothesis for the increased capture efficiency in the slug tests may be that the dirt better sticks to the effusion plate upon impact at higher loading rates due to compaction of the dirt. Barringer et al. [32] showed that small rust particles tended to clump together when subjected to centrifugal forces acting on the particles. Similarly, when particles have high loading rates the dirt particles are subjected to forces causing the particles to clump together. The large clumps of dirt are not able to pass through the cooling configuration. The slug feed mechanism results lend themselves to this theory because in this feed method, the effusion plate experiences high levels of dirt loading at a few discrete moments in time. The continuous feed tests experience a lower dirt loading rate, but over the course of the entire experiment. However, the slug feed mechanism also endured a decrease in capture efficiency with increased dirt introduction. This trend may be attributed to the fact that the dirt can accumulate only up to a height of 2.5D, or the thickness of the spacer plate. As a result, the high capture efficiency of the slug feed could not be maintained with higher amounts of dirt introduction and a finite amount of space. The slug feed's capture efficiency could be anticipated to approach that of the continuous feed.

Dirt thickness follows the same trend as capture efficiency between the two feed mechanisms. Figure 2.7 shows average capture efficiency and dirt thickness values in the area of interest, in all directly comparable tests. Directly comparable, here, refers to tests with experimental conditions that were identical between the two feed mechanisms. Specifically, Table 2.3 shows that for all unheated tests, dirt amounts of 105, 420, and 1260 mg and BFMs of 1.33, 2.82, and 4.32% were completed for both feed mechanisms. To compare the two feed mechanisms, the capture efficiencies and dirt thicknesses from the aforementioned six test conditions were averaged. These averages are shown in Figure 2.7. Both capture efficiency and dirt thickness averages were lower in the case of the continuous feed mechanism.

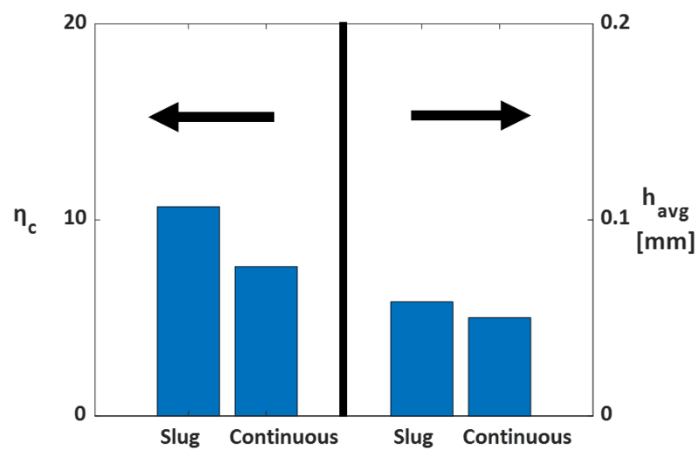

Figure 2.7. Average capture efficiency and dirt thicknesses over all directly comparable tests between the slug and continuous feed mechanisms. Experiments were conducted at room temperature.

Even the laterally averaged dirt thickness traces resulting from each of the two feed mechanisms are different as depicted by Figure 2.8. The peaks of dirt that lie underneath the impingement jets build up higher and more pointed in the slug feed tests. This difference in dirt traces also lends itself to the hypothesis that increased dirt loading rate increases the capture efficiency of the effusion plate.

Overall dirt patterns on the effusion plate are not significantly affected by the difference in feed mechanisms. Figure 2.9 depicts the effusion plate comparing the two feed types side by side with 105 mg of dirt introduced on top and 420 mg below. The light-colored areas correspond to dirt on the plate surface. The continuous feed test pictures on the right were taken in different lighting, resulting in the necessity to desaturate the pictures. In both amounts of dirt introduction, the two feed types create near identical dirt patterns. In the 105 mg case, pictures A and B, the dirt accumulates on the effusion plate in a peak and ridge formation. The peaks form underneath the impingement jets with ridges forming between them. The area of the effusion plate surrounding the peaks is swept clean by the wall jet region of the impingement jet. Pictures C and D of Figure 2.9 display the effects of 420 mg of dirt introduction. Here the ridges are more pronounced and build up higher. Although major dirt patterns between the two feed mechanisms are the same, the dirt ridges are slightly thicker in the slug feed case as shown in Figure 2.7. This difference is too small to be noticed in the top-down view of Figure 2.9.

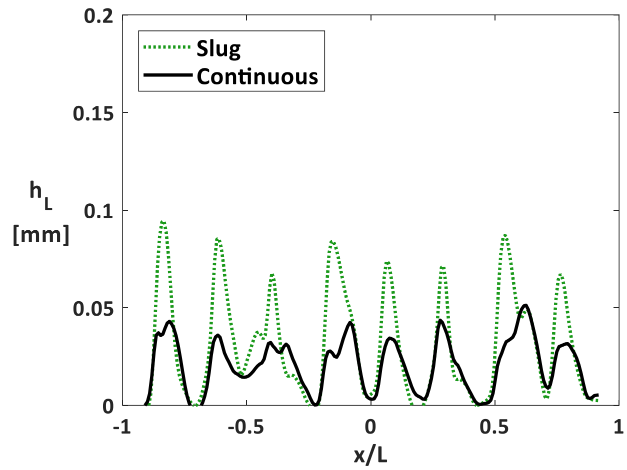

Figure 2.8. Laterally averaged dirt thickness traces along the effusion plate when 105 mg of dirt is introduced. Experiments were conducted at room temperature and at BFM of 3.42%.

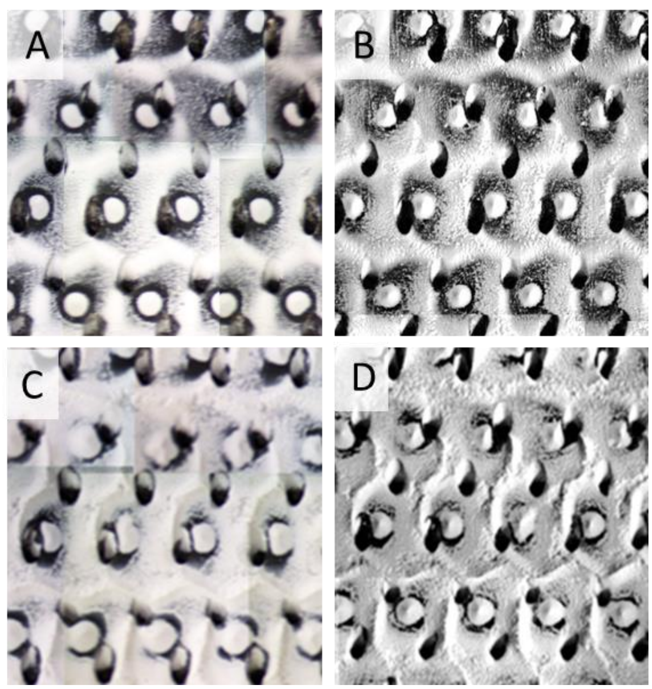

Figure 2.9. Post-test microscope pictures depicting dirt accumulation patterns on the effusion plate 's upstream face. Dirt accumulation corresponds with the light-colored surfaces. Pictures A and B show slug and continuous feed tests, respectfully, with 105 mg of dirt introduced. Pictures C and D show slug and continuous feed tests, respectfully, with 420 mg of dirt introduced. Experiments were completed at room temperature and at a BFM of 3.42%.

2.7 Effect of Backflow Margin

Tests of varying back flow margin were conducted when comparing the two feed mechanisms under unheated conditions. Figure 2.10 shows the capture efficiency of both the slug and continuous tests at four different BFMs. There was no difference between the two feed types at the lower BFM conditions; however, the capture efficiency associated with each feed began to diverge once the BFM was increased further than 2.82%.

In the case of continuous feed, capture efficiency actually peaked and began to decline at a BFM of about 2.82%. This shift in trends can also be seen in Figure 2.11 where the tests run at 4.32% BFM had much different accumulation patterns on the effusion plate compared to tests run at 1.33% BFM. Pictures C and D of Figure 2.11 show that the dirt was swept off the effusion plate directly underneath the impingement jets, save for small, flat deposits of dirt. This cleaning of the effusion plate occurred as a result of the increased BFM and, therefore, flowrate, causing a decline in capture efficiency. The increased BFM also contributed to the accumulation of ridges between dirt peaks. Pictures A and B with a BFM of 1.33% only show the peak structures of dirt with very little remnants of ridges. At the increased BFM, pictures C and D show the smaller, flattened peaks, as well as major dirt coverage in the form of ridge patterns between peaks.

In the case of the slug feed mechanism, the capture efficiency did not peak with increased BFM. However, one hypothesis behind this discrepancy is that, as previously stated, the slug feed at a higher loading rate leads to higher capture efficiency.

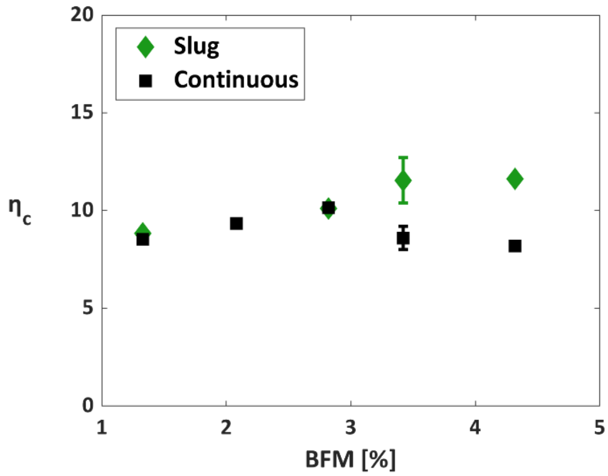

Figure 2.10. Average capture efficiencies for each of the two different feed mechanisms with uncertainty bars at two points. Experiments were conducted at room temperature with 420 mg of dirt introduced.

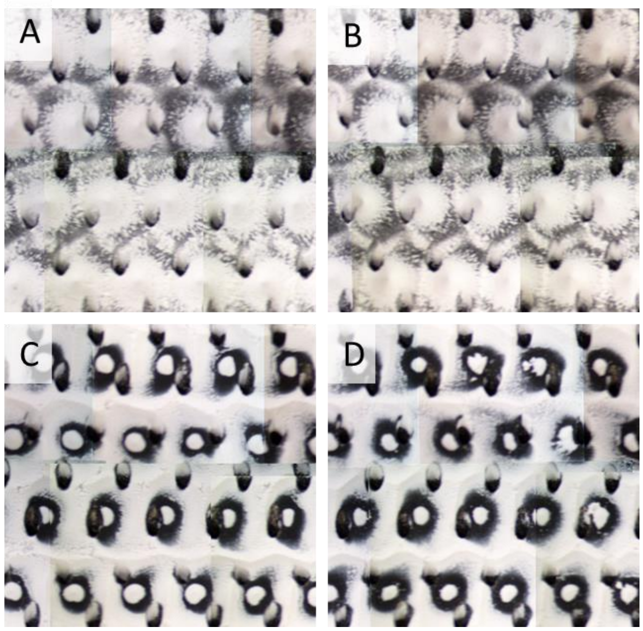

Figure 2.11. Post-test microscope pictures depicting dirt accumulation patterns on the effusion plate ‘s upstream face. Dirt accumulation corresponds with the light-colored surfaces. Pictures A and B show slug and continuous feed tests, respectfully, at a BFM of 1.33%. Pictures C and D show slug and continuous feed tests, respectfully, at a BFM of 4.32%. Experiments were completed at room temperature and with 420 mg of dirt introduced.

When compared to each other, the laterally averaged dirt thickness traces of Figure 2.12 and Figure 2.13 further pointed to a decreasing trend of dirt thickness peaks and capture efficiency with increasing BFM. In the experiments conducted at a BFM of 1.33%, most dirt thickness trace peaks exceed 0.1 mm and are close to 0.15 mm. Most peaks in the 4.32% BFM case are below 0.1 mm. The uniformity of peaks also varies with BFM. At 1.33% BFM, there are fewer laterally averaged dirt thickness trace peaks and much more resemble cone-like structures, whereas, in the 4.33% BFM case, there are many secondary peaks along the trace albeit less pronounced. This phenomenon can again be attributed to by the increased flowrate resulting from increased BFM. When the impingement jets impact the effusion plate at higher velocities, the dirt peaks do not build up as much and the area surrounding the peaks is swept clean. The dirt thickness traces then display lower and less uniform peaks. The change in peaks is not to be confused with overall dirt thickness. With the appearance of ridges on the effusion plate, the average dirt thickness does not change with a variable BFM.

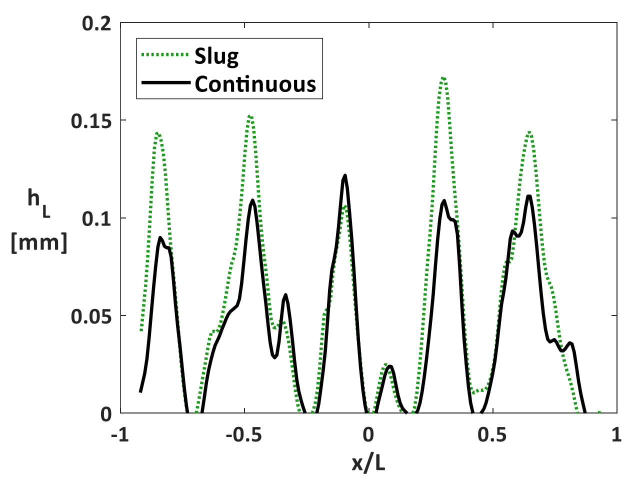

Figure 2.12. Laterally averaged dirt thickness traces along the effusion plate. Experiments were conducted at room temperature, at a BFM of 1.33%, and with 420 mg of dirt introduced.

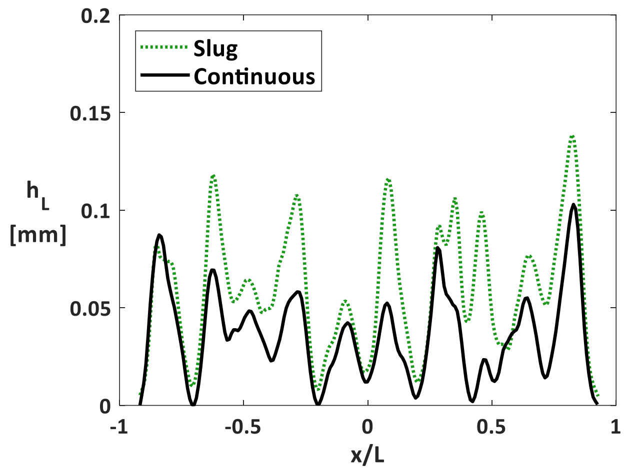

Figure 2.13. Laterally averaged dirt thickness traces along the effusion plate. Experiments were conducted at room temperature, at a BFM of 4.32%, and with 420 mg of dirt introduced.

2.8 Effect of Temperature

Variable dirt amounts and BFM tests were also conducted with continuous feed at high temperatures by placing the double pass heat exchanger inside a kiln. During heated tests, the effusion plate reached 760°C and the mainstream flow reached 620°C as indicated in Table 2.3.

As shown by Figure 2.14, increasing the temperatures of the hot plate and mainstream flow increases capture efficiency and average dirt thickness relative to the unheated tests. This increased capacity for the dirt to stick to the effusion plate at higher temperatures agrees with the findings from Hsu et al. [14] and Lundgreen [33]. Lundgreen [33] explains that increased temperatures in deposition film cooling studies decrease the normal coefficient of restitution, further confirming the dirt's ability to readily stick to the effusion plate at higher temperatures. The dirt particles soften, allowing increased deformation and therefore increased contact surface area when impacting the effusion plate.

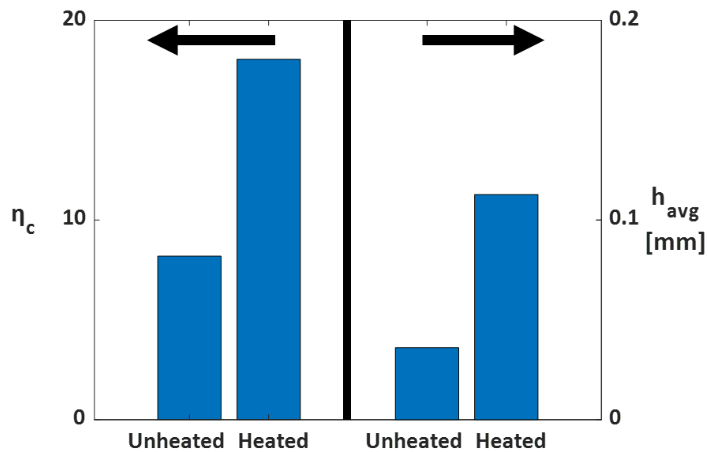

Figure 2.14. Capture efficiency and average dirt thickness for both heated and unheated conditions. Experiments were conducted with the continuous feed mechanism, at a BFM of 4.32%, and with 420 mg of dirt introduced.

Specifically, the shift from unheated to heated tests increased capture efficiency by about a factor of two. On the other hand, average dirt thickness was increased by a factor of about 3. This difference infers that during heated tests, a higher percentage of dirt that is captured by the effusion plate lays within the region of interest; the only area where dirt thickness is measured. A higher percentage of dirt captured within the region of interest also agrees with the notion that the dirt is stickier at higher temperatures. The stickier dirt will adhere to the effusion plate as soon as it passes through the impingement holes, in the area of interest, rather than impacting the effusion plate and then being blown around, potentially outside the area of interest.

Figure 2.15 shows the effect of temperature on dirt accumulation patterns for two different back flow margins. The dirt only accumulates in the peak formation in pictures B and D, leaving the rest of the effusion plate clear. The increased stickiness of the dirt causes it to stick upon impact with the effusion plate, right underneath the impingement jets. This phenomenon is also seen when comparing pictures C and D. At the high BFM in picture C, the dirt peaks are flattened, surrounded by clear areas under the impingement jets and dirt ridges in between. Picture D shows the dirt peaks growing outward in the higher BFM heated test with ridges just beginning to form in a couple rows. Laterally averaged dirt thickness traces in Figure 2.16 show the dramatic increase in dirt peak heights as a result of raised test temperatures that cannot be seen from the top-down view.

Raising the temperature of the effusion plate and mainstream flow also changes the way BFM interacts with dirt deposition. Figure 2.17 shows the capture efficiencies of variable BFM tests conducted at both heated and unheated conditions. As previously shown by Figure 2.10, capture efficiency peaked and eventually declined as BFM was increased in unheated conditions. However, during heated tests, capture efficiency is seen to increase with BFM as a result of the greater stickiness of the dirt. One theory to explain this difference, similar to the theory explaining slug feed capture efficiency at varying BFMs, is that upon further increase of BFM, even heated tests would eventually reach a point where capture efficiency began to decline. This shift would only occur at even higher BFMs in order to overcome the increased dirt stickiness.

Contrary to capture efficiency, although average dirt thickness increases in the high temperature case, Figure 2.18 shows that it remains independent of BFM. Again, this constant average dirt thickness is attributed to the appearance of ridges between peaks and the decrease in peak heights when the backflow margin is increased as shown in Figure 2.16.

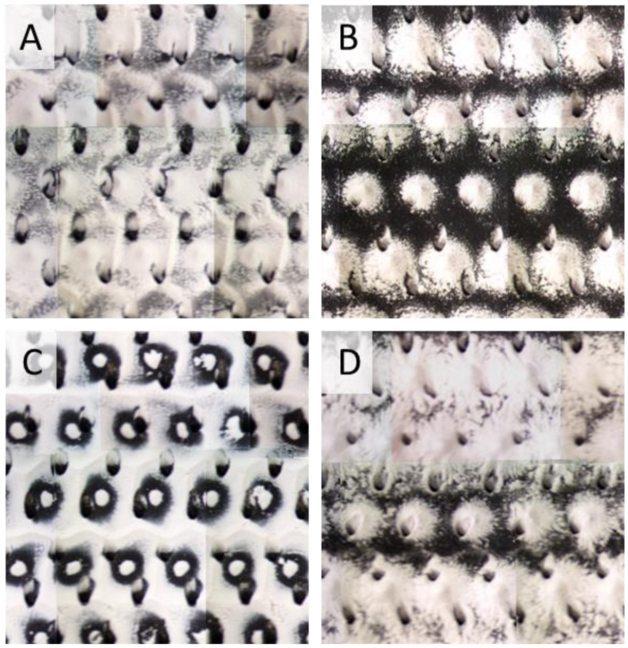

Figure 2.15. Post-test microscope pictures depicting dirt accumulation patterns on the effusion plate 's upstream face. Dirt accumulation corresponds with the light-colored surfaces. Pictures A and B show unheated and heated tests, respectfully, at a BFM of 2.08%. Pictures C and D show unheated and heated tests, respectfully, at a BFM of 4.32%. Experiments were completed with 420 mg of dirt introduced.

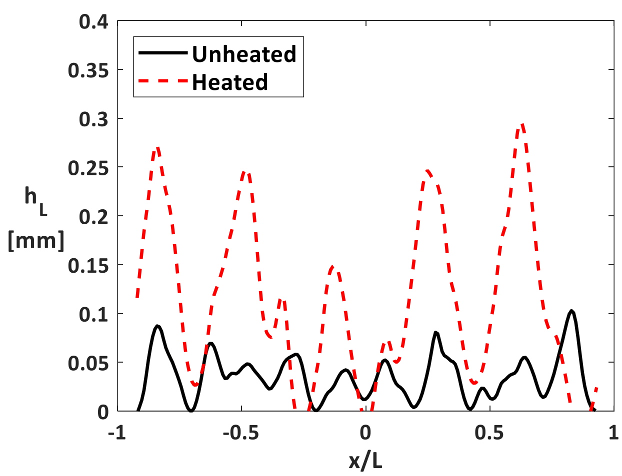

Figure 2.16. Laterally averaged dirt thickness traces. Experiments were conducted with continuous feed, a BFM of 4.32%, and 420 mg of dirt introduced.

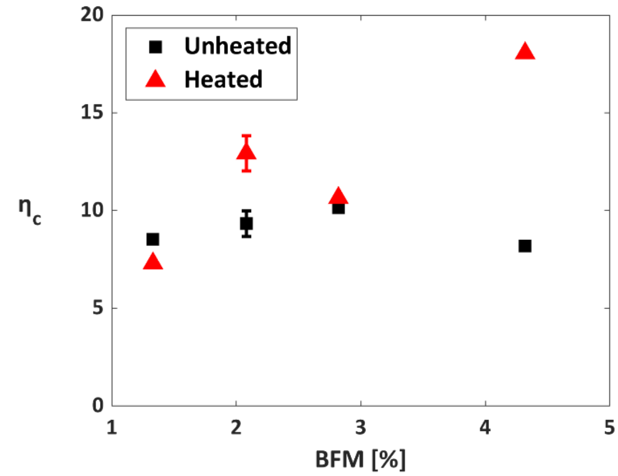

Figure 2.17. Average capture efficiencies at a variable BFM with uncertainty bars at two points. Experiments were conducted with continuous feed and 420 mg of dirt introduced.

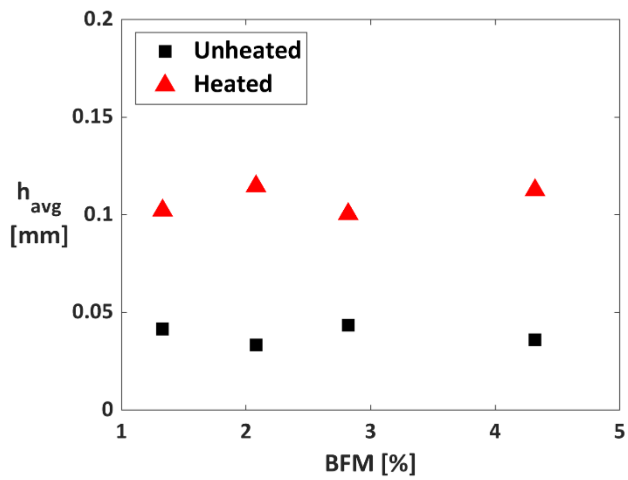

Figure 2.18. Average dirt thickness at a variable BFM with uncertainty bars at two points. Experiments were conducted with continuous feed and 420 mg of dirt introduced.

2.9 Conclusions

Two different feed mechanisms were used to perform dirt deposition tests in a double-walled cooling configuration in order to build an understanding as to how dirt loading can affect dirt deposition. Impingement and effusion plates of the double-wall cooling geometry were fixed to a double-pass heat exchanger in which dirt-laden flow impacted the faces of the plates.

Variable dirt introduction and variable BFM experiments were conducted for each of the two different feed mechanisms for unheated conditions. The slug feed resulted in high capture efficiencies that decreased with increasing amounts of dirt introduction. Continuous feed tests conducted with the same experimental conditions resulted in lower capture efficiencies than the slug feed and remained constant with the introduction of more dirt. These results lend themselves to the theory that dirt loading rate affects dirt accumulation. The larger loading rate at discrete moments during a slug feed test resulted in increased capture efficiency and dirt thickness. Despite this difference, overall dirt patterns, as shown by microscope pictures and laterally averaged dirt thickness traces, were not affected by the change in feed mechanisms. The dirt accumulated in peak and ridge formations in both cases; higher with the slug feed.

Experiments conducted with varying back flow margins showed that increasing BFM increased capture efficiency up to a certain point. Eventually, capture efficiency peaked with continued increases in BFM in the case of continuous feed. This decline in capture efficiency was confirmed by microscope pictures in which higher BFM experiments showed signs of impingement jets sweeping away dirt on the effusion plate directly underneath. Higher BFM experiments also caused the decline of dirt peak heights and increased in ridge formations on the effusion plate. These transformations brought a massive change in dirt patterns but did not affect average dirt thickness in the area of interest as a result of cancelling each other out.

With the continuous feed, experiments of varying dirt introduction amount and BFM were also conducted at high temperatures. Increased capture efficiencies and dirt thicknesses resulting from heated tests were caused by an increased capacity of the dirt to stick to a hotter effusion plate with hotter air flowing through.

These results contribute to the knowledge of dirt deposition in double-wall cooling configurations and the effects of varying conditions such as the method by which dirt is introduced into a turbine component. This knowledge can assist in predicting dirt accumulation levels and patterns within turbine cooling configurations where deposition is a growing problem.

Chapter 3

Impact of Ceramic Matrix Composite Topology on Friction Factor and Heat Transfer

Abstract

Ceramic matrix composites (CMCs) are of interest for hot section components of gas turbine engines due to their low weight and favorable thermal properties. To implement this advanced composite in a gas turbine engine, characterizing the influence of CMC's surface topology on heat transfer and cooling performance is critical. However, very few published studies have reported the flow and heat transfer effects caused by this unique surface topology. This study is an experimental and computational investigation to evaluate the effect of weave orientations, relevant to CMC surfaces, on the resulting pressure loss and convective heat transfer within an internal channel. The weave pattern was additively manufactured as the walls of a scaled-up coupon containing a single channel. For each of the three weave orientations, bulk pressure losses and convective heat transfer coefficients were measured over a range of Reynolds numbers.

Scaling the pressure losses in terms of a friction factor and convective heat transfer coefficients in terms of a Nusselt number showed the importance of choosing the appropriate definition of the hydraulic diameter, which was particularly important for the friction factor. A coupon having one wall with the weave surface increased pressure loss and heat transfer compared to a smooth wall with the largest increases occurring when the CMC weave strands were perpendicular to the flow. Friction factor augmentations were much higher than heat transfer augmentations. When adding the weave to a second channel wall, pressure loss and heat transfer were further increased. Orienting the CMC strands perpendicular to the flow consistently showed the largest augmentations in heat transfer over a smooth channel, but at a much higher pressure loss penalty than that seen with the CMC strands parallel to the flow.

3.1 Introduction

Ceramic matrix composites (CMC) have the potential to improve the efficiency of a gas turbine engine through enabling high firing temperatures while reducing the amount of coolant air required. CMCs are made up of ceramic fibers embedded in a ceramic matrix, helping to reduce the brittle nature of ceramics while maintaining ceramic's advantageous thermal properties. Low weight and high temperature capabilities give CMCs significant advantages over the incumbent nickel super alloys commonly used in today's gas turbines [34,35]. The use of CMC components within gas turbines has been found to reduce the weight, and therefore, increase thrust-to-weight ratio [36] as well as enable high power density and more efficient engines [37]. A parametric study by Tong [38] found that using CMC stator vanes in a two-stage high pressure turbine reduces thrust-specific fuel consumption by up to 1.5%. Additionally, a CMC combustor liner was found to reduce the landing-and-takeoff NOx emissions by over 40% due to lowering the required liner cooling [38].

With the ability to withstand high temperatures, the full impact of CMCs, including the resulting surface topology, need to be understood. One of many differences between CMCs and traditional cast turbine components is the inherent roughness created by the CMC's weave. This unique topology creates macro-roughness features that influence the aerodynamic and heat transfer performance. When delving deeper into the subject of this pattern topology, various weave orientations can induce different effects on cooling performance. The research in this study is unique because of the specific weave effects chosen as well as the approach to evaluate the effects on channel heat transfer and pressure loss.

3.2 Literature Review

As previously stated, CMCs have significant advantages over materials used in present gas turbine engines. Namely, the low weight and ability of CMCs to withstand high temperatures [34,35] can allow their use to enable more efficient engines [37,38]. Many studies have investigated the development of the mechanical properties of CMCs and their abilities to withstand harsh and high temperature environments. Zhu et al. [39] provides an overview of the development of CMCs, describing how the further progress of CMCs will result in a step increase in gas turbine temperature capabilities. Zhu et al. [39] also details mechanical properties such as tensile strength, elastic modulus, and rupture strength associated with a few different CMC fiber types. The oxidation and morphology of environmental barrier coated (EBC) and uncoated CMCs when exposed to high temperatures have been investigated by Alvin et al. [40]. Multiple studies have reported on the effects of high temperatures and thermal stresses on CMCs [39, 41,42]. Furthermore, Watanabe et al. [43,44] conducted studies demonstrating the capabilities of CMC vanes and blades in various cyclic loading and spin tests.

Despite the growing amount of research concerning the structural properties of CMCs, few published studies have focused on how the surface topology of a CMC weave can affect convective heat transfer performance. Unlike cast or machined surfaces, CMCs have a unique surface roughness in the form of woven ceramic fibers that have an effect on convective heat transfer. When studying the interaction between an impinging jet and an additively manufactured CMC weave pattern, Krishna et al. [45] observed an augmentation of Nusselt number for a weaved surface relative to that of a smooth surface. In their preliminary study, their results indicated a strong dependence of the heat transfer on the orientation of the CMC weave pattern relative to the impinging jet. In a later study, Krishna et al. [46] attributed the dominant effect on the heat transfer augmentation from their previous study [45] to additive manufacturing roughness rather than the actual CMC weave pattern. Using a machined surface to better match the weave pattern, heat transfer augmentation was determined to be within experimental uncertainty.

Wilkins et al. [47] investigated the effects of a CMC weave pattern on local heat transfer augmentation and boundary layer development for an external flow using a scaled up, additively manufactured 5-harness satin weave pattern. When the weave pattern was rotated such that the longer CMC strands were perpendicular to the flow, larger local variations in Stanton number results were observed compared to other weave orientations. However, area-averaged results showed little increase in overall heat transfer.

The majority of public CMC research has been reported on the development of this advanced material's structural properties. Using the 5-harness satin weave pattern provided by Nemeth et al. [48] and also used by Wilkins et al. [47], the current study is a unique investigation on the effects of a representative CMC weave on internal convective heat transfer and pressure drop. Our study aims to fill an important gap in considering the usage of CMCs for turbine applications.

3.3 Weave Pattern Geometry and Manufacturing

Single channel coupons with weave patterns on either one wall (1W) or two walls (2W) that were representative of a CMC surface were additively manufactured. To isolate effects of the weave pattern and avoid those caused by AM roughness, the weave pattern in this study was scaled up from traditional CMC fiber sizes by a factor of 3.8. Figure 3.1 shows the description of the coupons, starting with the coupon dimensions in Figure 3.1a. The weave surfaces of the internal channel walls were created by overlaying six adjacent repeating unit cells (RUCs) containing the weave. Depending upon the particular coupon, the weave was placed either on one wall or two walls of the channel marked by W, as shown by Figure 3.1b. The weave pattern investigated in this study was a 5-harness satin (5HS) weave described by Nemeth et al. [48] that was created in TexGen [49], a program that generates user defined weave patterns. The 5HS square weave RUC is shown by Figure 3.1c and 3.1d. Within the 5HS pattern, each of the five long tows are overlapped by one of the five cross tows once per RUC. Relative to the 5HS pattern in Nemeth et al. [48], the weave in this study was created with a slightly thicker fabric to produce more definition between the intersecting tows. Dimensions for the RUC are listed in Table 3.1 in terms of the average channel height (H) and width (W). The root mean square (RMS) roughness of the weave pattern was determined by fitting the design intent RUC to the AM RUC. The height differences between the AM weave surface and design intent were used to calculate the RMS roughness as shown by equation 3.1, where M is the number of data points along the weave surface. The RMS roughness of the weave was 0.04H.

$$RMS_w = \sqrt{\frac{1}{M}\sum_{i=1}^{M}(z_{surf} - z_{des})_i^2} \tag{3.1}$$

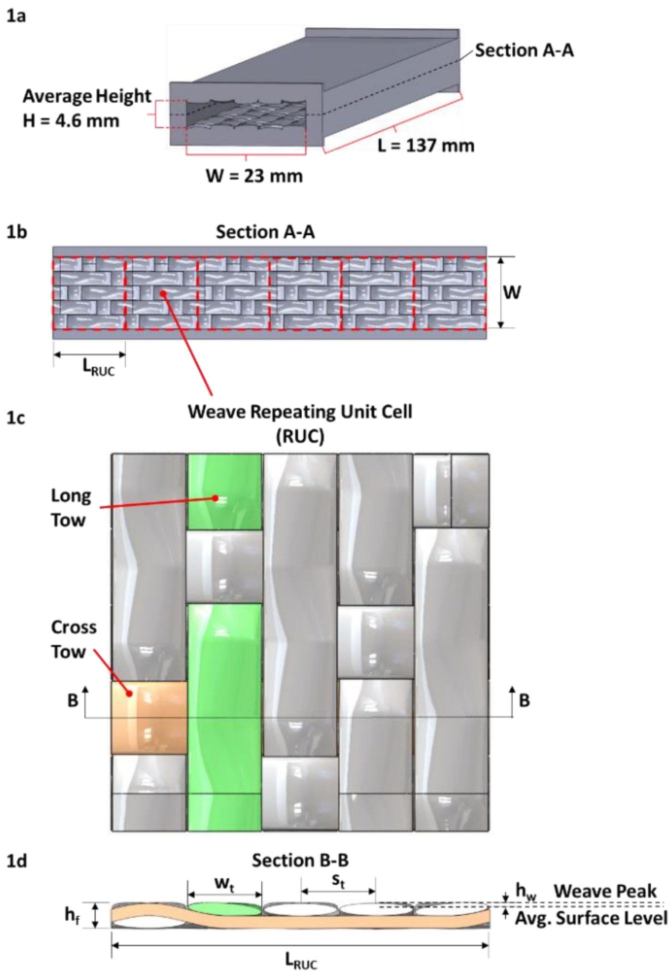

Figure 3.1. (1a) shows the coupon model with design channel dimensions. (1b) shows a cross section view of the bottom channel wall with a weave surface created by six adjacent weave RUCs. (1c) and (1d) show a top down view and side cross section view of the RUC.

Table 3.1. RUC Dimensions

Parameter	Size
RUC Length, L_{RUC}	1.0W
Tow Width, w_t	0.19W
Tow Pitch, s_t	0.20W
Fabric Height, h_f	0.32H
Weave Peak, h_w	0.04H

All coupons were additively manufactured (AM) in halves with a state-of-the-art direct metal laser sintering machine. Each coupon half consisted of the entire coupon length and one of the large internal walls as shown by Figure 3.1b. The halves were printed with the weave pattern facing upward so that AM printing effects would be minimized. All coupons were printed from Inconel 718, except for the 90-1W coupon, which was made of Hastelloy X. All coupon halves were removed from the build plate and cut to the proper dimensions by wire electrical discharge machining (EDM). Finally, each coupon half was welded to its counterpart along section A-A seen in Figure 3.1a to finish the manufacturing process.

All channel aspect ratios were 5:1 for these studies. A total of seven coupons were printed as shown in Table 3.2 where the naming convention consists of the weave angle (0°, 45°, and 90°) as well as whether the weave was on one or two channel walls. Three different weave orientation angles and two different weave alignments were chosen in this study. The weave orientations are shown in Figure 3.2. In the 0° orientation, the long weave tows that cover most of the surface were parallel to the direction of channel flow. In the 90° orientation, the long tows were perpendicular to the flow. All channel aspect ratios were 5:1.

Table 3.2. Coupon Geometry Types

Coupon Name	Weave Orientation	Weave Walls	Aspect Ratio
0-1W	0°	1 Wall	5
45-1W	45°	1 Wall	5
90-1W	90°	1 Wall	5
0-2W-A	0°	2 Aligned Walls	5
0-2W-S	0°	2 Staggered Walls	5
90-2W-A	90°	2 Aligned Walls	5
90-2W-S	90°	2 Staggered Walls	5

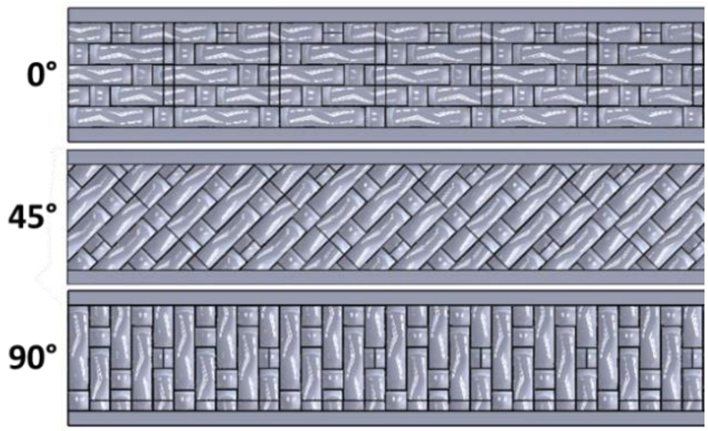

Figure 3.2. Top-down view of the bottom channel walls for the three different weave orientation angles.

Also evaluated in this study was the weave alignment for the 0° and 90° orientations by placing the weave patterns on both the top and bottom channel walls. The channel sidewalls were smooth. In the aligned cases, the top and bottom wall weave patterns were identical. In the staggered cases, the top wall weave was offset from the bottom by $L_{RUC}/2$, as shown in Figure 3.3.

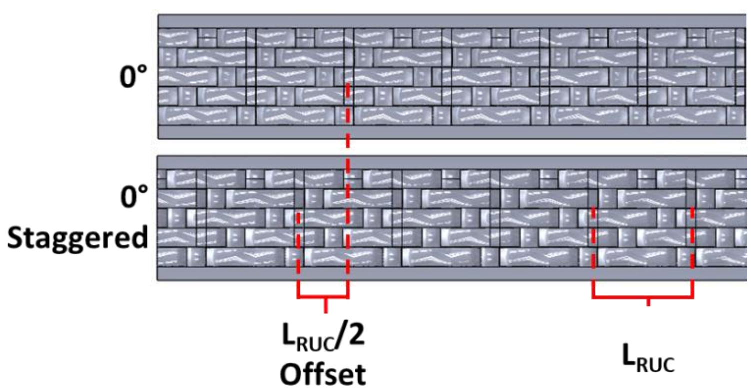

Figure 3.3. Top-down view of the 0° weave channel walls for the aligned case (top) and for the staggered weave pattern.

Upon completion of the manufacturing, the as-built channel dimensions were calculated by taking computed tomography (CT) scans of each test coupon. Specialized software was used to calculate channel perimeter, cross sectional area, surface area, and wall thickness. However, with complex weave surface topology, calculating these parameters can be done in a number of different ways. As such, two calculation methods were implemented in this study. The first method, referred to as Method 1, consisted of calculating the hydraulic diameter (D_h) at various cross-sectional slices down the length of the channel as shown by equation 3.2 and Figure 3.4a, where N equals the number of slices. The cross-sectional area of each slice was calculated by determining the size and number of CT pixels within the open channel area of the slice image. The perimeter of each slice was calculated by the number of pixels along the edge of the open channel area.

$$D_h = \frac{1}{N} \sum_{i=1}^{N} 4 \frac{A_{c,i}}{P_i} \tag{3.2}$$

Method 2 for calculating D_h was based on placing a rectangular channel in which the rectangle's bounds lined up with the average minimum to maximum height of the channel's walls as shown by Figure 3.4b. The average surface height of each internal channel wall was determined using the CT scan data.

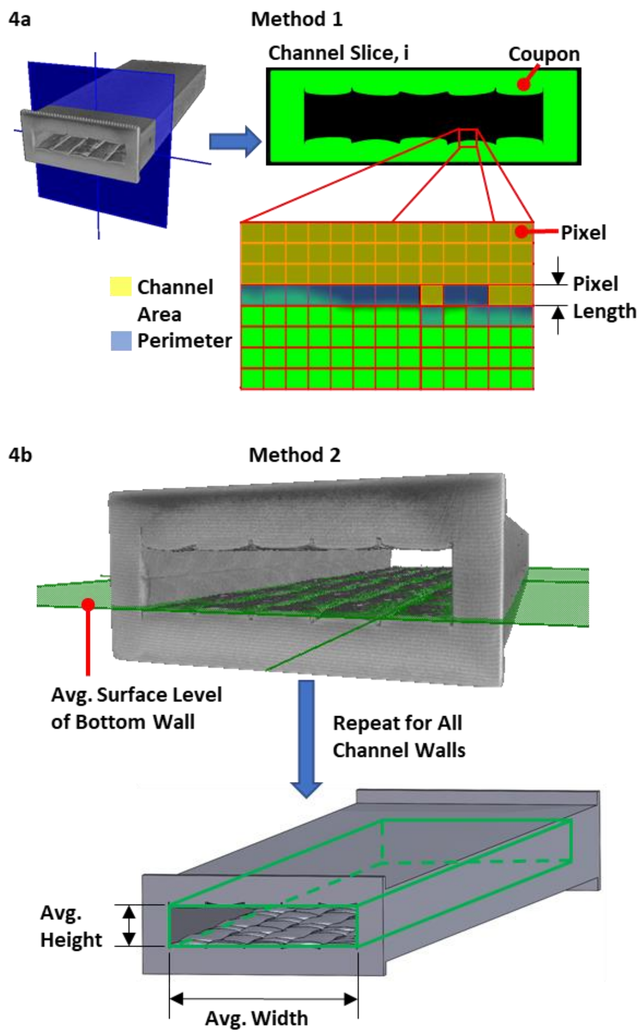

Figure 3.4. Different methods for calculating D_h using (4a) Method 1 with cross sectional slices of the channel and (4b) Method 2 with a fixed rectangular shape.

The main point of interest within the two parameter calculation methods was the substantial difference in D_h. This disparity is seen in Figure 3.5 where the D_h calculated using Method 2 is consistently larger than that of Method 1 for each of the coupons tested. The percent difference between D_h calculation methods across each coupon ranges from 7% in the 90-2W-S coupon and up to 20% in the 0-2W-A coupon. The presence of the weave pattern surface adds additional surface are due to the valleys of the weave surface. This relative change causes Method 1, which calculates D_h at numerous cross sections and takes an average value for the channel, to yield a smaller D_h compared to Method 2. The differences in the D_h of each method have a large impact on the friction factor results as discussed in the results section of this paper.

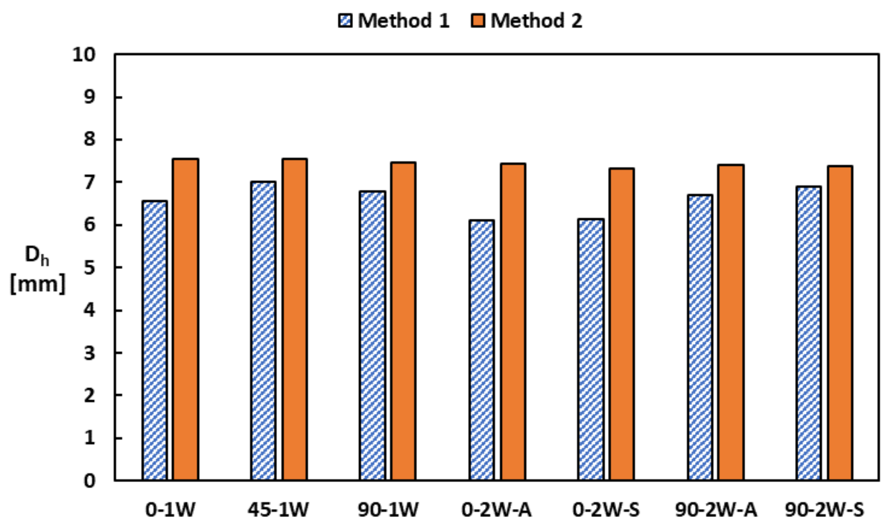

Figure 3.5. D_h of each coupon geometry using calculation methods 1 and 2.

3.4 Experimental Setup and Methodology

Pressure losses and convective heat transfer experiments were conducted using a test rig similar to those used by Stimpson et al. [50] and Snyder et. al [51]. Figure 3.6 depicts a cross sectional view of the test rig consisting of two plenums located upstream and downstream of the test coupon. The upstream plenum supplies the inlet of the coupon with a uniform velocity flow. The downstream plenum provides a rapid expansion of the flow as it exits the channel.

The pressure loss for each coupon was measured using static pressure taps placed upstream of the coupon inlet and downstream of the exit to measure the pressure change across the coupon. Inlet and exit losses of the plenums were calculated and accounted for to obtain an accurate pressure decrease across the coupon alone. A smooth coupon with pressure taps at the inlet and exit was used to determine the plenum contraction and expansion loss coefficients. The mass flowrate was measured with a laminar flow element and temperature measurements were taken at the direct inlet and exit of the coupon. Subsequently, friction factor was calculated.

Bulk convective heat transfer coefficients were measured using a method similar to that outlined by Stimpson et al. [50]. An electrical resistance heater was placed between a copper block and foam insulation, as shown in Figure 3.6. The copper block was used in order to exert a constant surface temperature boundary condition on the test coupon. Thermal contact resistance was minimized by applying a thin layer of thermally conductive paste between the coupon and copper blocks. Thermocouples placed in the plenums and foam blocks were used to calculate the conduction losses, which were below 7% of the total input power for all cases.

The convective heat transfer coefficients were determined by calculating the amount heat transferred to the fluid and the log mean temperature difference. The amount of heat transferred to the fluid resulted from the heat input from the heaters minus any conductive losses. For validation purposes, the outlet temperature measurement was compared to a first law analyses and found to agree by equal to or better than 8% for all cases.

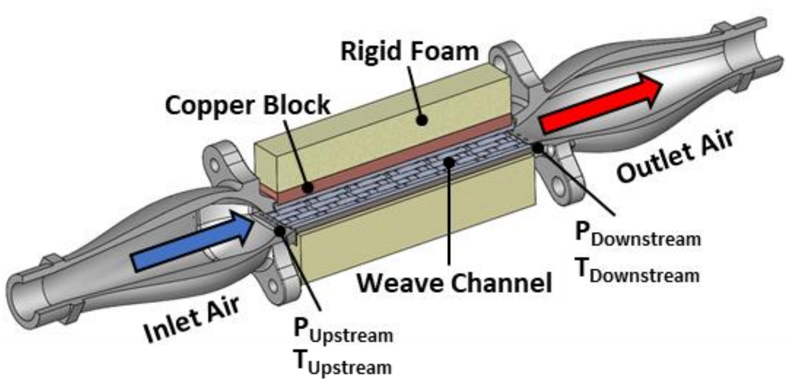

Figure 3.6. Schematic of experimental rig used for pressure drop and heat transfer experiments.

3.4.1 Experimental Uncertainty

Measurement uncertainty was determined by the analysis method described by Figliola and Beasley [52]. Pressure drop was the largest contributor to uncertainty for friction factor. The uncertainty for friction factor was below 9% for all Reynolds numbers (Re). The uncertainty in Reynolds number was below 2%. Flow temperature measurements were the largest contributor to Nusselt number uncertainty, which was less than 10% for all cases.

3.5 Computational Fluid Dynamics Setup

A conjugate, computational fluid dynamics (CFD) study using a Reynolds Averaged Navier Stokes (RANS) approach was conducted on the same seven coupon geometries to gain further insights into the experimental results. STARCCM+ [53] was used for the conjugate simulations. The turbulence model implemented in these steady RANS simulations was the realizable k-ε model. A segregated flow solver was also implemented.

Boundary conditions of the simulations included a velocity inlet of the channel and a pressure outlet at the exit. The pressure outlet for all coupons was set to atmospheric pressure, the same as the experiments. All CFD simulations were conducted at Re = 40,000. In the heat transfer simulations, uniform heat sources were added to the top surface of the upper copper block and the bottom surface of the lower copper block to match experiments. The exposed outer sidewalls of the copper blocks and coupon were set as adiabatic, which was also similar to the experiments having foam blocks on the side.

Each of the four components of the coupon model was meshed separately as shown in Figure 3.7. The copper blocks, channel, and fluid domain all used a polyhedral mesher with the fluid domain also using prism layer meshing at the near wall regions. Meshing the weave pattern, especially with the deep gaps between the tows, proved to be fairly difficult and a few key details were necessary to create a proper mesh. The CAD models of the copper blocks and coupons were imported into STARCCM+ [53] and then the fluid domain was created by conducting a Boolean subtraction from the internal channel of the coupon. When meshing the fluid domain and coupon, increasing the number of cell faces based on the surface curvature was important for capturing the sharp changes in surface resulting from gaps in the weave tows. Each coupon was between 650,000 and 1,200,000 cells due to geometry differences. The fluid domain mesh was intentionally varied in order to determine the simulations' degree of grid independence. Nominal mesh sizes for the fluid domain were between 7M and 11M cells. When the mesh size was increased from 10M to 15M cells, Nusselt number calculations varied by a maximum of 2% in one geometry due to the mesh change and by less than 1% in the other six coupons.

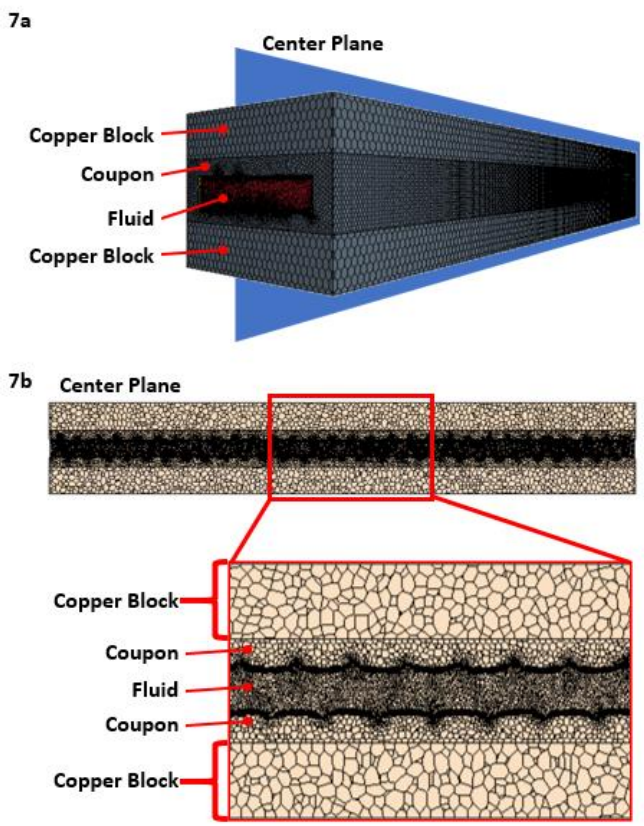

Figure 3.7. (7a) shows an example of the entire simulation meshes. (7b) shows views of the mesh at the center plane of the models.

3.6 Impact of Hydraulic Diameter Calculation

The friction factor and Nusselt number (Nu) of rectangular channels containing varying orientations and alignments of a 5HS weave surface were measured experimentally and predicted through CFD. Within experimental testing, each coupon geometry was tested between Re = 5,000 and 50,000. The experimental tests were benchmarked through the use of a smooth channel coupon in the same rig. The smooth channel data was compared with the Colebrook correlation [54] in equation 3.3 for hydrodynamically smooth ($K_s = 0$) channels through the Reynolds numbers tested.

$$\frac{1}{\sqrt{f_0}} = -2\log_{10}\left(\frac{K_s}{3.7D_h} + \frac{2.51}{Re\sqrt{f_0}}\right) \tag{3.3}$$

For the smooth channel testing, the experimental data agreed with the correlation to within 11% at Re = 5,000 and to within 5.2% beyond Re = 7,400 as shown in Figure 3.8.

In heat transfer testing, the benchmark data was compared with the Gnielinski correlation [55] as given by equation 3.4, for a hydrodynamically smooth ($K_s/D_h = 0$) pipe through the Reynolds numbers tested.

$$Nu_0 = \frac{\left(\frac{f_0}{8}\right)(Re\text{-}1000)Pr}{1+12.7\left(\frac{f_0}{8}\right)^{0.5}\left(Pr^{2/3}\text{-}1\right)} \tag{3.4}$$

The smooth coupon testing agreed to within 11% of the correlation at Re = 10,000 to within 1.5% at Re = 50,000 as shown in Figure 3.9.

For the coupons containing the weave surface, the friction factors are heavily dependent on the method chosen for calculating each coupon's D_h. By manipulating the Darcy-Weisbach equation, the friction factor can be shown to scale with D_h to the fifth power. This significance can be seen in the friction factor results of Figure 3.8. Here, friction factor of the 0° one wall (0-1W), 0° two wall aligned (0-2W-A), and 0° two wall staggered (0-2W-S) coupons using both Methods 1 and 2, previously described, for the D_h calculations are shown along with the smooth channel benchmark. The differences in D_h values cause up to a 62% difference between average friction factor values of a single coupon. As a result of the lower D_h determined through Method 1, friction factors were lower than that of Method 2, even producing values that fall below the Colebrook correlation of a smooth coupon.

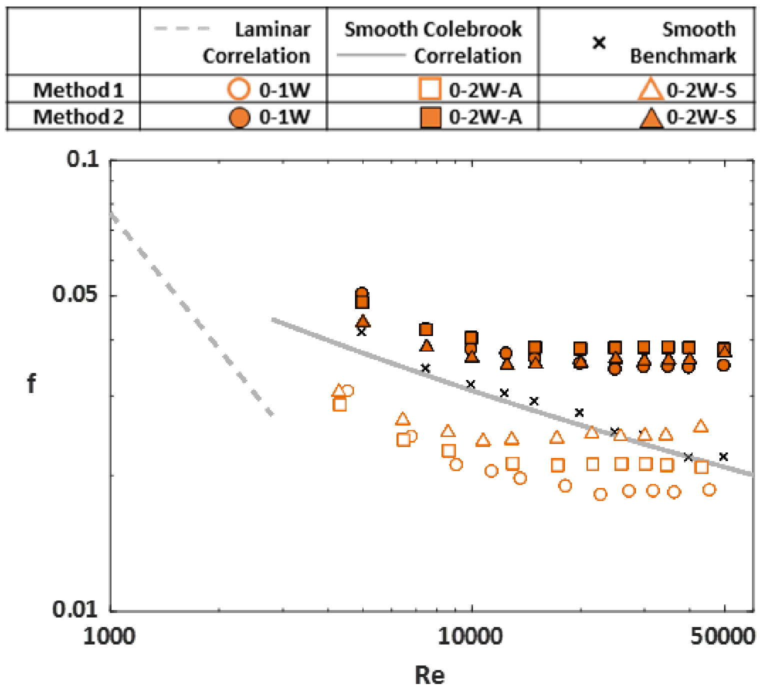

Figure 3.8. Friction factor over a range of Reynolds numbers for the 0° coupons using Dh calculation methods 1 and 2.

When investigating Methods 1 and 2 for the heat transfer scaling, the resulting Nusselt number values are not as significant as in friction factor. Figure 3.9 shows Nusselt numbers using each method for the 0° orientation coupons. Similar to friction factor, the Method 2 D_h results in higher Nusselt number values. However, the percent difference between the two methods is only as high as 33%.

These results show the importance of choosing an appropriate scaling dimension such has hydraulic diameter. In the case of this weave pattern, the wetted surface of the valleys in the weave are a significant influence, which are being captured using Method 1 resulting in D_h values that are low. As will be shown from the CFD predictions, these valleys result in recirculation regions in the valleys of the weave surfaces that result in the bulk of the channel flow only in the core region. As such, the D_h values that were chosen to be representative of the weave geometry to scale the pressure loss and heat transfer data were calculated with Method 2. All of the data in the following sections used Method 2.

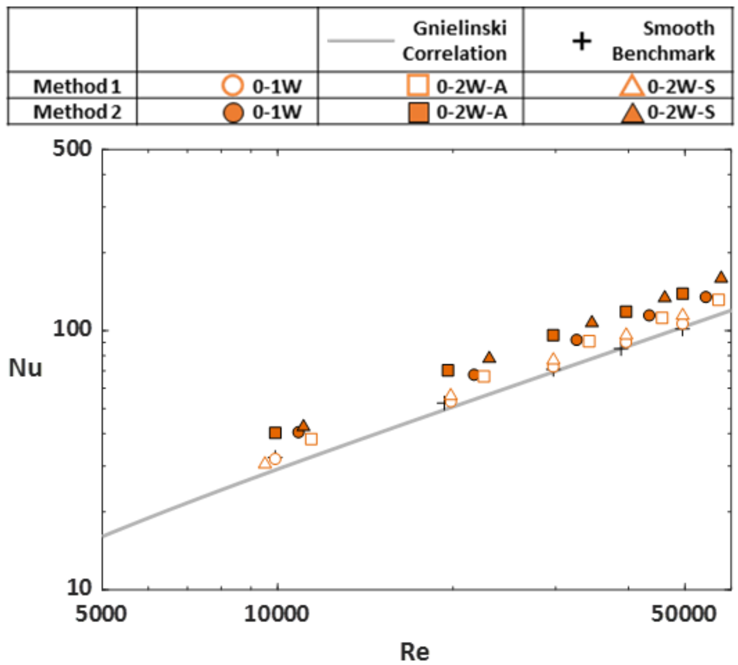

Figure 3.9. Nusselt number over a range of Reynolds numbers of the 0° coupons using Dh calculation methods 1 and 2.

3.7 Weave Orientation Effects for One Wall Coupons

This section reports on the results for coupons containing only one wall with a weave pattern to isolate the effects of weave orientation. This removes additional effects of weave alignment as seen in the case of two weave walls that will be discussed in the next section. Both friction factor and Nusselt number results, obtained from pressure loss and heat transfer measurements, are reported using Method 2 as described previously for calculating D_h. CFD predictions are also compared and used to further explain the results.

The effect of weave orientation for the one wall coupons can be seen in Figure 3.10, showing the benchmark measurement along with the experimental and CFD predictions for the three weave orientations evaluated. At low Re, there is little difference between the weave orientations; however, as Reynolds number increases beyond Re > 10,000 the 90° orientation shows the highest friction factor, followed by the 45°orientation while the 0° orientation has the lowest friction factors. The CFD results show a similar trend at Re = 40,000, with the 90° orientation having the highest friction factor, but CFD overpredicts friction factor for all weave orientations.

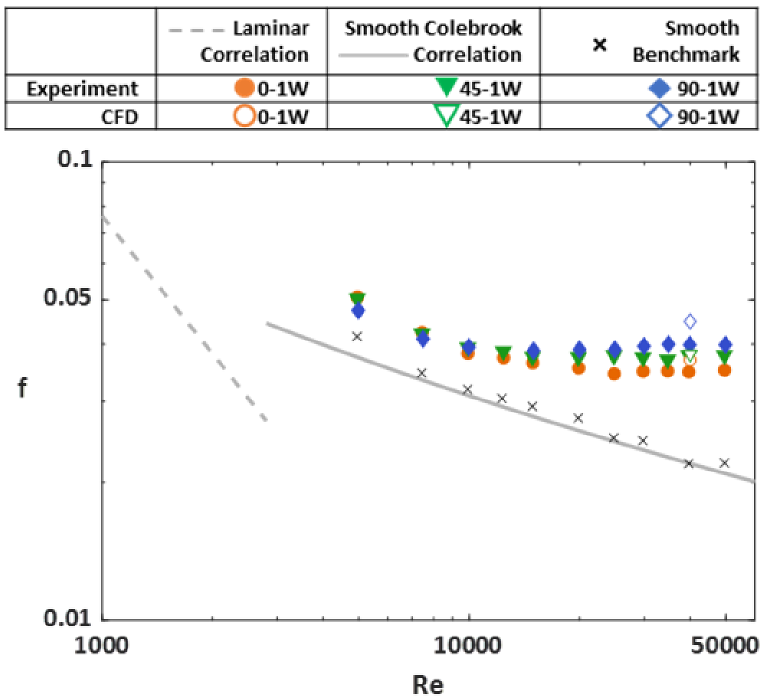

Figure 3.10. Friction factor for a range of Reynolds numbers for the coupons containing one weave wall.

Augmentation values as a function of Re were also calculated, based on f_0, defined by equation 3.3, for a smooth channel wall ($K_s = 0$). These augmentation results can be seen in Figure 3.11. For Re < 10,000, augmentation values are at a minimum of 1.2 for all three weaves but then increased with increasing Re, with the 90° orientation showing the highest augmentation. As seen in Figure 3.10, the smooth benchmark friction factor decreases with increasing Re, as predicted by the Colebrook correlation, while the friction factors for the coupons having a weaved surface remain constant with increasing Re. These constant friction factors are consistent with behavior seen in rough internal channel flows. The weave acts as surface roughness resulting in constant friction factor at sufficiently high Re, with the 90° orientation having the highest "roughness", and the 0° having the lowest. The CFD predictions at Re = 40,000 agree in trends, but both the 90° and 0° are both over-predicted in terms of augmentation.

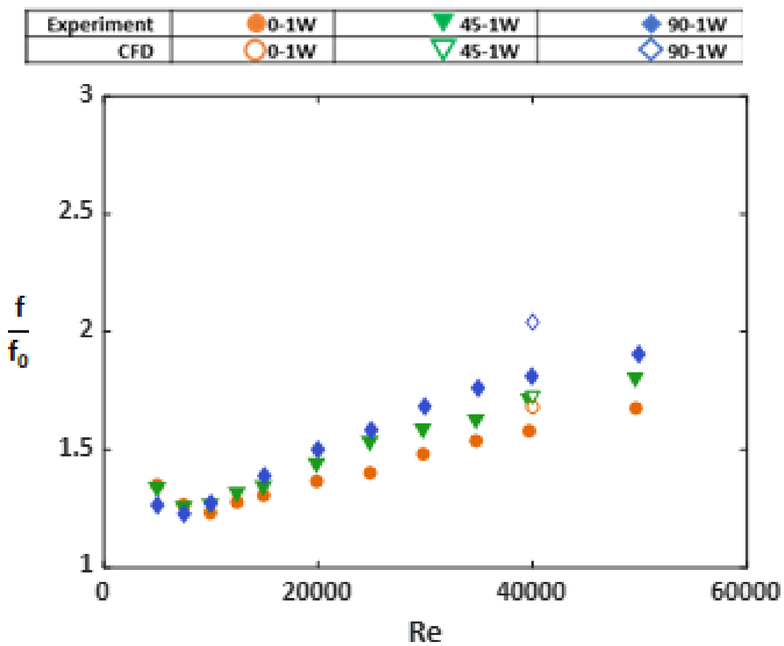

Figure 3.11. Friction factor augmentation for a range of Reynolds numbers of the coupons containing one weave wall.

Heat transfer results, in terms of Nu, can be seen in Figure 3.12, which shows increases in Nu relative to a smooth wall for all weave orientations. The 0° and 45° orientations have the same heat transfer performance, while the 90° orientation is slightly higher than the other two orientations. The CFD simulations underpredict Nu, but match the same trends seen by the experimental results at Re = 40,000.

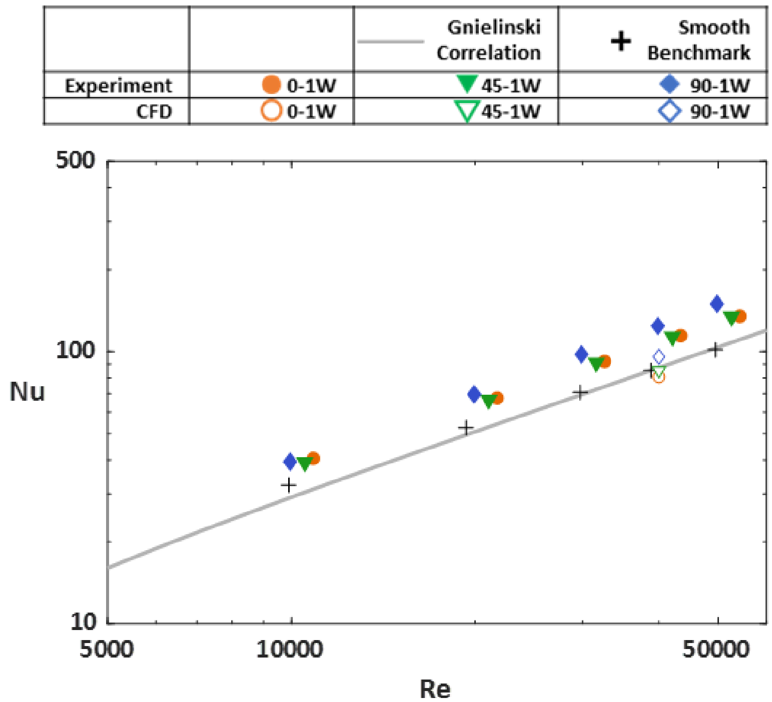

Figure 3.12. Nusselt number for a range of Reynolds numbers of the coupons containing one weave wall.

Heat transfer augmentation values as a function of Re were calculated, based on Nu_0, defined by equation 3.4, using smooth wall friction factor values from equation 3.3. These augmentation results can be seen in Figure 3.13. In contrast to friction factor augmentation levels, the heat transfer augmentations are significantly lower and remain nearly constant with Reynolds number. This phenomenon of higher friction factor augmentations than heat transfer augmentations is a consistent trend in many different internal channel flows and will be discussed further in a later section. The data in Figure 3.13 indicates only a slight increase in augmentations for the 90° weave and a slight decrease seen in the 0° and 45° orientations for increasing Re.

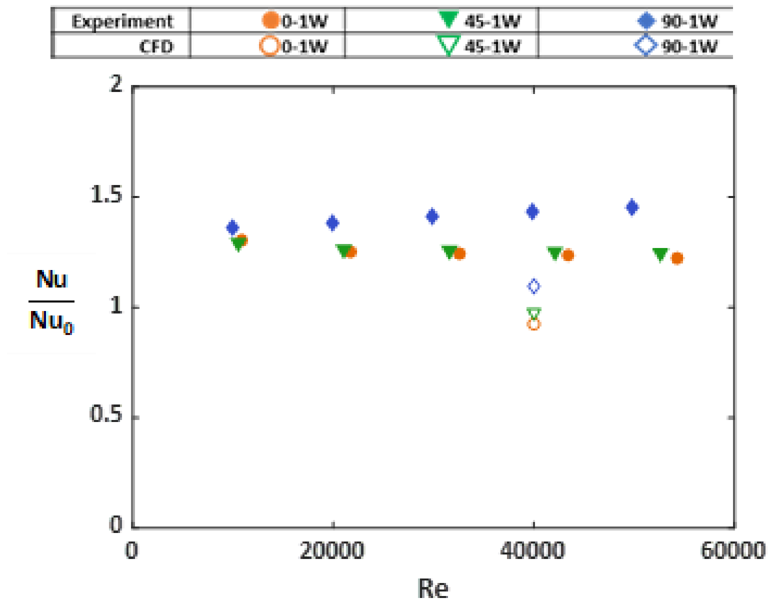

Figure 3.13. Nusselt number augmentation for a range of Reynolds numbers of the coupons containing one weave wall.

Figure 3.14 shows predictions of local Nu along the weave wall for the 0°, 45°, and 90° orientations, respectively. As indicated from the experiments, higher Nusselt numbers result from the 90° weave in comparison to the others. For the 0° weave, the windward edge of the weave provides a stagnation location for the flow resulting in high heat transfer which is amplified for the 90° case resulting in much higher heat transfer overall as compared to the other weave cases.

Another observation from the Nusselt number contours is that streaks of low Nusselt numbers occur for both the 45° and 90° cases shown in Figures 3.14b and 3.14c. To better understand the heat transfer phenomena, Figure 3.15 shows cross sectional views of the flow field, with secondary flow vectors and contours of normalized temperature (θ) for the 0°, 45°, and 90° orientations, respectively. For the 0° weave in Figure 3.15a, warm fluid remains near the wall with an unmixed core flow and a lack of coherent vortical structures. However, for the 90° weave in Figure 3.15c, distinct vortical structures can be seen in the secondary flow vectors that develop into cells of cooler and hotter fluid regions. These differences in secondary flow patterns result in the low and high Nu streaks seen in Figure 3.14c.

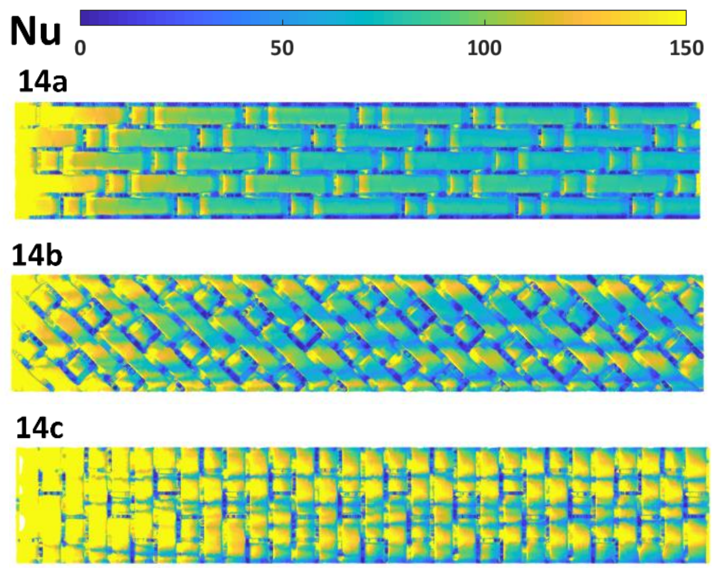

Figure 3.14. Top-down view of local Nusselt number contours for Re = 40,000 on the full length of the one weave wall coupons for the (14a) 0° orientation, (14b) 45° orientation, and (14c) 90° orientation.

Figure 3.16 shows centerline streamwise views of normalized temperature (θ) within the fully developed region of each channel as well as expanded views of cavity regions for the 0°, 45°, and 90° orientations, respectively. For the 0° and 45° in Figures 16a and 16b, stagnant flow recirculation regions can be seen, where the warm fluid remains in the recessed cavities formed by the interlacing cross sections of the long tow and cross tow weaves. However, in Figure 3.16c for the 90° case, a recirculation region is not apparent with the warm fluid being drawn into main channel flow. The 90° orientation weave has structures that are distinctly different from those seen in the 0° orientation and 45° orientation which contributes to an increasing augmentation in Nusselt number with Reynolds number as seen in Figure 3.13.

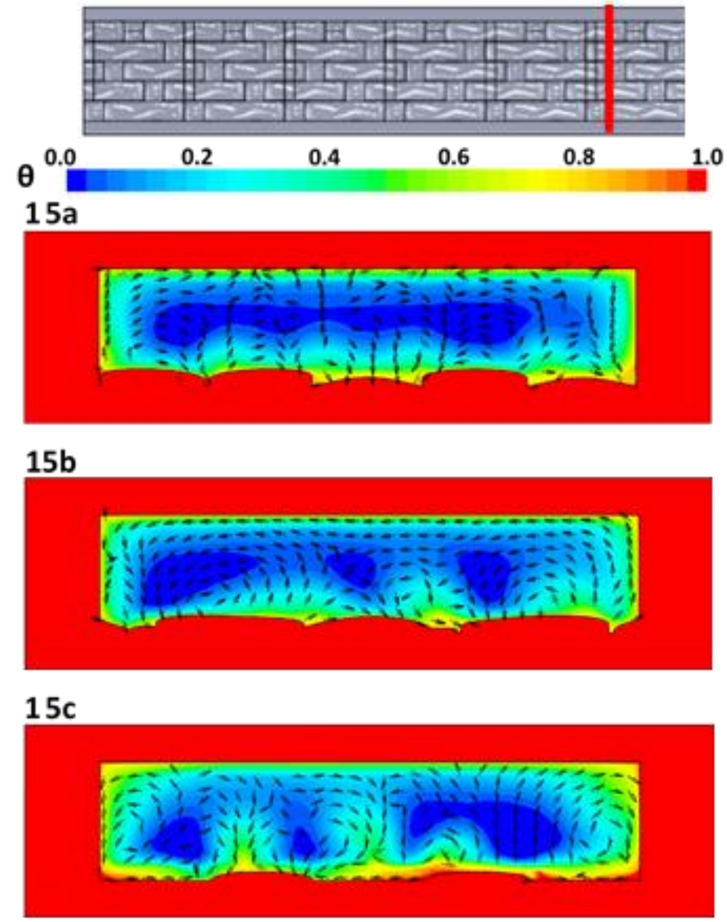

Figure 3.15. Cross-sectional view of normalized temperature at Re = 40,000 at an x/L distance of 0.9 for the (15a) 0° orientation, (15b) 45° orientation, and (15c) 90° orientation.

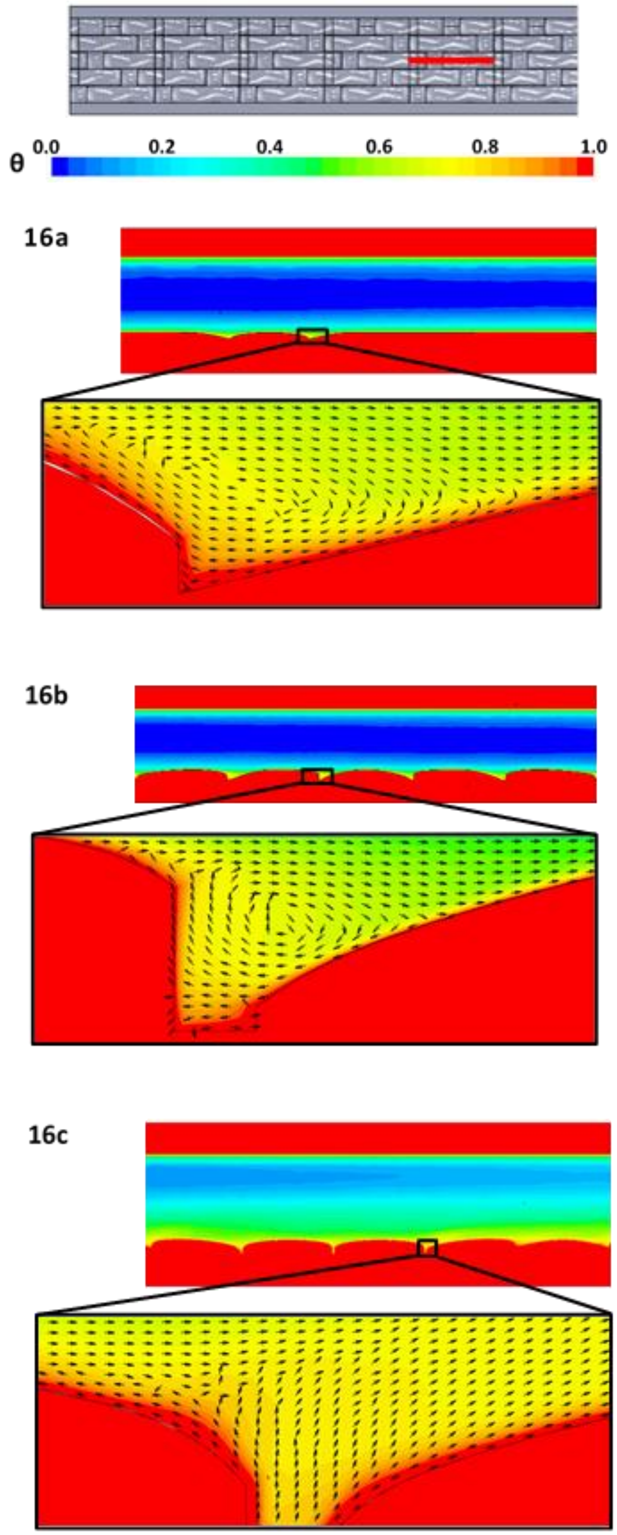

Figure 3.16. Normalized temperature fields at Re = 40,000 in the fully developed region of 0.67 < x/L < 0.83 including expanded views for the (16a) 0° orientation, (16b) 45° orientation, and (16c) 90° orientation.

3.8 Weave Alignment Effects for Two Wall Coupons

After isolating the one wall effects of the weave, coupons were constructed that included weaves on the two walls having the largest surface areas. In addition, the effect of weave alignment was evaluated. The aligned weave patterns were identical on the top and bottom channel walls while the staggered weave patterns were offset by $L_{RUC}/2$. These studies were conducted for the 0° and 90° weave orientations.

Figure 3.17 shows the measured and predicted friction factor augmentation for all the 0° and 90° weave coupons including the one wall, two wall aligned (2W-A), and two wall staggered (2W-S) coupons. The results for the 0° weave indicate nearly the same augmentation levels between the one wall and two wall cases. The 90° two wall coupons, however, have significantly higher augmentation values as compared with the one wall coupons and have much higher augmentations than the 0° coupons, as expected.

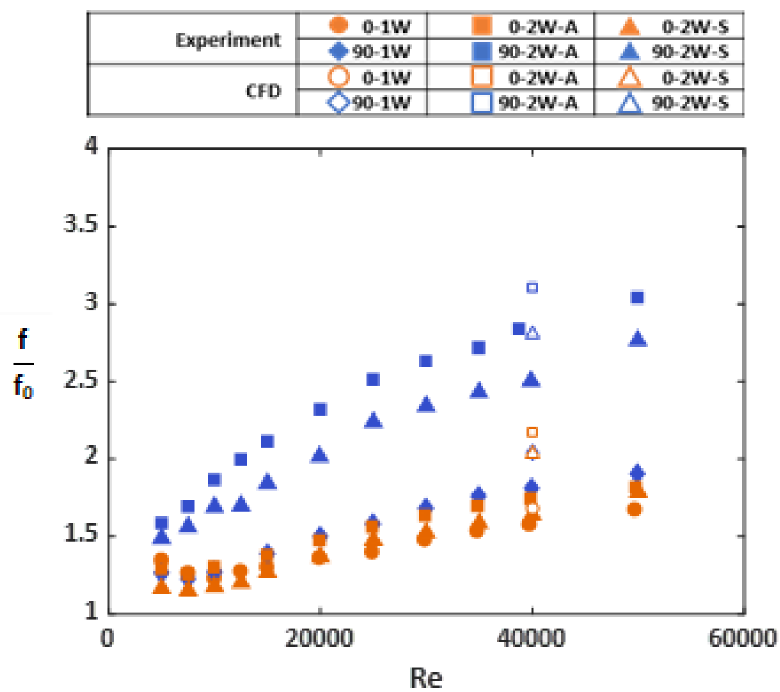

Figure 3.17. Friction factor augmentation over a range of Reynolds numbers of the 0° and 90° coupons containing one and two weave walls.

Another noticeable effect in Figure 3.17 is for the 90° case in terms of whether the weave is aligned or staggered. The aligned case has higher augmentations than the staggered arrangement. In contrast, there is only a small effect for the 0° case in terms of whether the weave is aligned or staggered.

As was stated, similar to the one wall results, the augmentation results indicate that the 90° orientation angle significantly increased friction factor augmentation for the two wall cases as compared with the 0° orientation. This difference was caused by the increased flow separation in the gaps of the 90° orientation long tows relative to the lesser separation at cross tow intersections in the 0° orientation. Also similar to the one wall coupons, the two wall coupons resulted in increasing friction factor augmentation with Reynolds number because the weaves function similar to rough surfaces in internal channel flow where friction factor is constant with Reynolds number.

As discussed, a clear result in Figure 3.17 is that the 90° two wall coupons resulted in a large step increase in friction factor augmentation over the 90-1W variant whereas the 0° two wall coupons caused only slight increases over their 0-1W counterpart. This difference is due to the 90-1W coupon having a larger friction factor augmentation than the 0-1W coupon. Therefore, adding a second wall with a 90° weave had a more significant impact than adding a second wall with a 0° weave. Friction factor augmentation values from the CFD also elaborate on this trend. Although CFD values generally overpredicted the experimental results, adding a second wall with a 90° weave caused a more significant increase in friction factor augmentation compared to the 0°. The 90-1W experimental augmentation of 1.9 at Re = 50,000 increased to 3.0 and 2.8 for the 90-2W-A and 90-2W-S coupons, respectively. For the 0° coupons, the friction factor augmentation increased from 1.7 at Re = 50,000 in the 0-1W coupon to 1.8 and 1.8 for the 0-2W-A and 0-2W-S coupons, respectively.

When comparing the two wall coupons in Figure 3.17, for both weave orientations in experiments and CFD, the cases where the weave patterns were aligned resulted in larger augmentations than the staggered weaves. Differences in weave alignment can be explained by evaluating the CFD results in Figure 3.18 which shows normalized temperature contours with velocity vectors at the centerline entrance regions of the 90-2W-A and 90-2W-S coupons. Near the top and bottom walls of Figure 3.18a, the aligned case indicates accelerated flow near the walls. However, Figure 3.18b shows an accelerated flow only near the bottom wall due to the staggering. Near wall velocity differences in the entrance region can be attributed to the initiation of the weave surface. In the aligned case, the weave was initiated at the front of a long tow across the span of the channel. As a result, the flow area contracted resulting in accelerated flow near the wall as it moves across the first tow in the channel. In the staggered case in Figure 3.18b, the bottom wall weave was initiated at the front of a long tow, but the top weave started in the center of a long tow. Consequently, the flow area near the bottom wall contracts, but the flow near the top wall expands as the downstream side of the long tow recedes into the channel wall. The decreased near wall velocity on the top wall of the staggered cases results in relatively lower shear stress and consequently pressure drop (lower friction factor augmentations) as compared to the aligned cases.

For the measured heat transfer results, the two wall coupons resulted in higher Nusselt number augmentations compared to the one wall coupons as shown by Figure 3.19 for both weave orientations. Overall, the heat transfer augmentations were not as high as the friction factor augmentations similar to the one wall results. The same trend of Nusselt number augmentation being lower than friction factor augmentation was found in Stimpson et al. [50] for heat transfer within additively manufactured microchannels. The weave roughness, especially in transitions between weave tows where the boundary layer is tripped, significantly affected friction factor, but did not cause enough mixing in the bulk of the flow to have as large of an effect on Nusselt number. When comparing Nusselt number augmentations of the aligned and staggered cases in Figure 3.19, differences in weave alignment caused very little change in heat transfer. For the 90° angle, the aligned case only showed an average augmentation increase of 3% over the staggered while for the

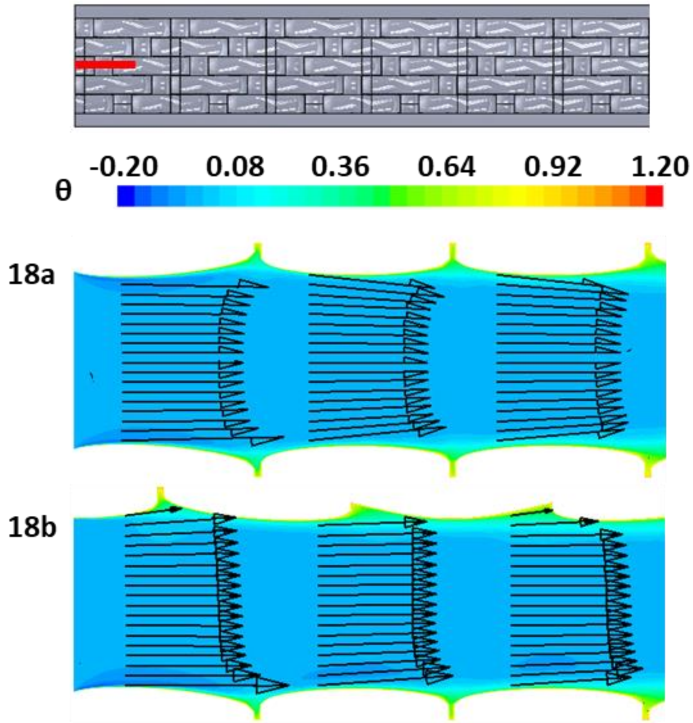

Figure 3.18. Normalized temperature contours with velocity vectors at the centerline of the channels between x/L of 0 and 0.1 with Re = 40,000. Figure (18a) shows the 90-2W-A coupon and (18b) shows the 90-2W-S coupon.

0° angle, there was an average percent difference of less than 1% between aligned and staggered cases. This trend is similar to that seen in friction factor augmentation where the 90° aligned and staggered cases showed larger differences than the 0°. However, Nusselt number augmentation differences were lower than friction factor augmentation differences between the aligned and staggered coupons.

Insignificant changes in Nusselt number augmentation were also seen in the CFD where there was less than a 1% difference between the aligned and staggered cases for both weave orientations. Although much more subtle than friction factor, the slight differences in Nusselt number augmentation for the 90° two wall coupons are explained by the same flow contractions and expansions caused by differing initiations in the weave patterns. The decrease in Nusselt number augmentation of the 90-2W-S coupon is caused by the decrease in flow velocity near the

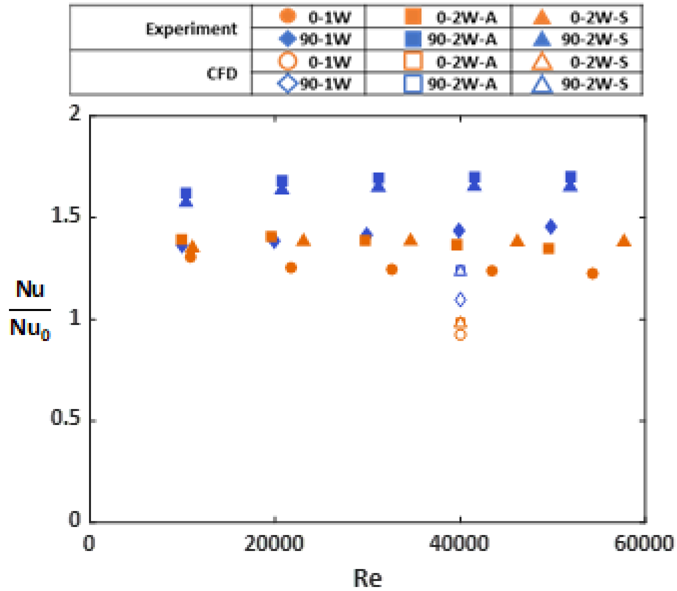

Figure 3.19. Nusselt number augmentation over a range of Reynolds numbers of the 0° and 90° coupons containing one and two weave walls.

top wall as shown in Figure 3.18b. The temperature contours of Figure 3.18 show decreased fluid temperatures near the walls where the flow accelerated, thereby increasing the fluid and surface temperature difference in those areas and increasing the amount of local convective heat transfer. On the top wall of Figure 3.18b, the flow had lower velocity than the bottom wall and did not decrease in temperature, comparatively reducing local Nusselt number.

The pressure drop and heat transfer results of this study were also compared to additively manufactured microchannels from Stimpson et al. [50] and parallel rib channels from Park et al. [56]. The ribbed channels were comprised of two ribbed walls along the width and smooth walls along the shorter side walls. All of the ribs were spaced by p/e = 10. The aspect ratios (AR) of the coupons being compared were 5 for the 5HS weave channels, 2 and 4 for the ribbed channels, and 2.3 and 2.1 for the microchannels. Figure 3.20 shows friction factor augmentation versus Nusselt number augmentation of the scaled up 5HS weave geometries, rib channels, and additive microchannels. The data taken for the rectangular microchannels is shown for a similar Reynolds number range up to Re = 20,000 [50] while the rib channels were from 10,000 to 60,000 [56].

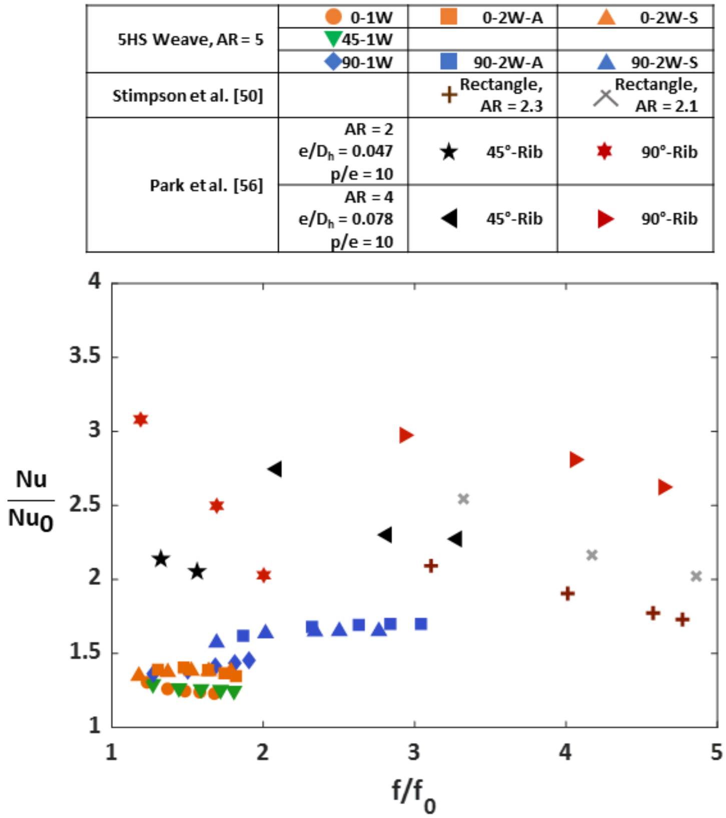

Figure 3.20. Nusselt number and friction factor augmentations of all weave geometries compared to additively manufactured microchannels from Stimpson et al. [50] and ribbed channels from Park et al. [56]. Aspect ratios of the weave channels are all 5. Aspect ratios of the ribbed channels are 2 and 4. Aspect ratios 2.3 and 2.1 of the microchannels are named L-1x-In and M-2x-In, respectively, in Stimpson et al. [50].

In Figure 3.20, the 5HS weave, the 90° two wall channels attained the highest Nusselt number augmentation and also the highest friction factor augmentation for the weave coupons. In fact, the relatively small increase in Nusselt number augmentation from the 90° two wall coupons cost a large increase friction factor augmentation.

The friction factor augmentation difference in the rib angles was much larger than the differences seen in the 5HS weave as shown in Figure 3.20. Note the 45° rib was able to achieve the same Nusselt number augmentation as the 90° rib at low friction factor augmentation before dropping below the 90° rib at AR = 4. With the 5HS weave, the same trend was present. When comparing to the rectangular microchannels with additive roughness [50], the weave channels generally exhibited lower Nusselt number augmentation and much lower friction factor augmentation. As a result of these comparisons, the weave pattern is shown to exhibit unique pressure drop and heat transfer performance relative to other types of internal roughness.

3.9 Conclusions

Experimental and computational studies assessed the effects of a woven surface pattern, representative of a CMC surface, on pressure loss and convective heat transfer performance within an internal channel. Experimental coupons were additively manufactured with differing orientations of a 5HS weave pattern overlaid onto the walls of rectangular channels. Pressure drop and heat transfer were measured through the channels over a range of Reynolds numbers from 5,000 to 50,000. CFD predictions were made on the same channels at Re = 40,000 for further understanding of the weave surface effects.

The friction factor and Nusselt number scaling highlighted the significance of an appropriate hydraulic diameter for the complex weave geometry. In using a method that fully accounted for the valleys of weave an artificially high wetted perimeter resulted due to the valley weaves. The data indicated that it was most suitable to use a rectangular channel that was fit to the average wall heights of the weave.

In the 0° orientation, the long tows of the 5HS weave resulted in lower friction factor and Nusselt numbers than in the 90° weave orientation where the long tows were perpendicular to the flow direction. Flow fields predicted through CFD showed flow separations within the valleys of the weave resulting in large pressure losses.

Heat transfer coefficients were also measured to be higher in the case of the 90° weave relative to the 0° weave; however, augmentations were much lower than the friction factor augmentations. The flow fields indicated that the nearly stagnant flow regions within the valleys of the weave led to poor flow mixing. In general, increases in local Nusselt number occurred on the upstream sides of weave tows while decreases occurred at the flow separation regions on the downstream sides of weave tows and in the gaps between weave tows. Local Nusselt number contours showed streaky patterns for the 45° and 90° weave orientations resulting from secondary flow patterns in the channel.

The effects of two weave wall channels along with weave alignment were evaluated for the 0° and 90° orientations. For both orientations, adding a second weave surface increased friction factor and Nusselt number augmentations. These increases were more significant for the 90° weave because of the increased flow separation and turbulent mixing associated with that orientation. Measurements indicated higher friction factor augmentations in the channels with the surface weave patterns aligned as opposed to staggered. CFD simulations showed that the differences in augmentation were most influenced by the initiation of the weave pattern at the channel inlet, which was identified as the reason for the higher values for the aligned case. Nusselt number augmentation was not significantly affected by the initiation of the weave, with results showing little difference between the aligned and staggered weaves.

Overall pressure loss and heat transfer performance of the weave surfaces were compared to additively manufactured microchannels and rectangular channels with parallel ribs. The weave channels exhibited lower Nusselt number augmentation than the rib channels as well as the additively manufactured microchannels. Similar to the ribbed channels, the weave channels showed increased augmentation values in the 90° orientation compared to the 45°.

Results of this study contribute to the knowledge of weave surface topology, representative of CMC surfaces, on pressure drop and heat transfer within internal channel flow. This knowledge can help predict internal cooling performance of turbine components with relevant surface patterns such as those made of CMCs. These results can also be used by the designer to orient the weave pattern in a favorable direction within the component.

Chapter 4

Conclusions and Recommendations

Cooling technologies are essential to keeping gas turbine components functional while also playing a key role in turbine efficiency. These cooling technologies take on multiple forms including double-walled cooling schemes as well as internal cooling passages. In this thesis, the aforementioned cooling technologies were researched with regard to dirt depositions and the effects of weave surfaces on cooling performance, respectively.

In deposition testing, two different feed mechanisms were used to study the effects of dirt loading on accumulation levels and patterns in a double-walled cooling scheme. Capture efficiency, dirt thicknesses, and dirt patterns were reported for an impingement and effusion plate exposed to dirt-laden flow. Varying amounts of dirt and varying backflow margins tested with both the slug and continuous feed mechanisms at unheated conditions showed that dirt loading significantly affected deposition. The larger loading rates of dirt introduced at discrete moments in the slug feed method resulted in larger capture efficiency and dirt thickness than the continuous feed method which maintained a lower loading rate, but over the course of an entire test. Overall deposition patterns where dirt formed peaks and ridges between effusion holes were not affected by feed method. When backflow margin was increased, capture efficiency eventually decreased. This decline was caused by the impingement jets sweeping away dirt on the effusion plate at higher backflow margins. The thickness of dirt peaks declined, but the thickness of ridges increased, resulting in no net change in average thickness values. Heated tests were also conducted with the continuous feed mechanism and showed much larger capture efficiency and dirt thickness values due to the increased propensity of dirt to stick when softened by high temperatures.

In weave surface testing, pressure loss and heat transfer were measured over a range of Reynolds numbers for rectangle channels containing one or two 5HS weave surface walls. CFD simulations at Re = 40,000 were also conducted to gain further understanding of the physics behind experimental results. Three different orientations were studied by rotating the weave pattern overlaid onto the bottom channel wall by 0°, 45°, and 90°. The effects of adding a second weave surface for the 0° and 90° orientations were studied by placing an identical weave pattern on the top channel wall. When isolating the effects of different weave orientations, the 90° weave pattern, where long tows were perpendicular to the flow, resulted in the largest friction factor. CFD analysis showed large amounts of flow separation at the gaps between long tows causing large pressure losses compared to the lesser flow separation at the intersections between long and cross tows in the 0° orientation. The 90° orientation also resulted in higher Nusselt number than the other orientations, but augmentation values remained lower than those of friction factor. Local Nusselt numbers from the CFD showed that heat transfer was increased on the upstream sides of weave tows while decreases occurred on the downstream sides and also in the gaps between tows. In the weave tow gaps, flow was nearly stagnant and did not fully mix into the core of the channel. When adding the weave surface to a second channel wall, both friction factor and Nusselt number augmentations increased. Friction factor augmentations of the aligned cases were higher than those of the staggered due to the initiation of the weave pattern as shown by CFD. Nusselt number augmentations were not affected by the differing weave alignments. Friction factor and Nusselt number results of the weave geometries were also compared to those of ribbed channels and microchannels. In general, the weave surfaces resulted in lower Nusselt number augmentations than the ribs or microchannels. However, the effect of weave orientation angle was similar to the effect of rib angles where the 90° geometries resulted in larger augmentations in both channel types.

Overall, the results discussed in this thesis provide valuable contributions to their respective fields. This knowledge is useful to gas turbine designers when predicting the effects of deposition or choosing weave orientations for cooled gas turbine components made of CMCs.

4.1 Recommendations for Future Work

Additional studies expanding on the research included in this thesis can be done to gain further understanding on the relevant subjects. In regards to deposition, the present study investigated capture efficiency and dirt thickness on one specific double-walled geometry. Thermal imaging of the effusion plate at the beginning and end of a test could be conducted to capture the effect of deposition on adiabatic effectiveness. Additionally, varying particle sizes and impingement and effusion hole sizes could be tested to see what combinations of these variables cause the largest capture efficiency and flow blockage. A scaled-up effusion hole could also be tested with appropriate particle sizes to isolate and investigate deposition specifically within the effusion hole.

Expanding on weave surface testing, different types of weave patterns as well as different channel shapes containing a weave surface could be tested to gain broader understanding of how different geometries affect cooling performance. Adjusting weave tow heights or the heights of the channels would also be beneficial in studying the extent of the weave wall's flow effects on the opposing smooth wall.

Conducting research that combines the two subjects of deposition and weave surfaces would also provide unique and beneficial study to the field of gas turbine cooling. Interesting interaction between the roughness of the weave surface and particle deposition could be expected and this research would be very valuable as CMC turbine parts continue to develop and are exposed to airborne particles.

References

[1] Wessel, R. A., and Righi, J., 1988, "Generalized Correlations for Inertial Impaction of Particles on a Circular Cylinder," *Aerosol Sci. Technol.*, **9**(1), 29-60.

[2] Clum, C., Bokar, E., Casaday, B., and Bons, J. P., 2014, "Particle Deposition in Internal Cooling Cavities of a Nozzle Guide Vane - Part I: Experimental Investigation," GT2014-27150.

[3] Dunn, M. G., 2012, "Operation of Gas Turbine Engines in an Environment Contaminated With Volcanic Ash," *J. Turbomach.*, **134**(5), p. 051001.

[4] Moroianu, D., Karsllon, A., and Fuchs, L., 2004, "LES of the Flow and Particle Ingestion Into an Air Intake of a Jet Engine Running on the Ground," GT2004-53762.

[5] Grant, G., and Tabakoff, W., 1975, "Erosion Prediction in Turbomachinery Resulting from Environmental Solid Particles," *J. Aircr.*, **12**(5), pp. 471–478.

[6] Hamed, A., Tabakoff, W., and Wenglarz, R., "Erosion and Deposition in Turbomachinery," *J. Propuls. POWER*, **22**(2), pp. 350–360.

[7] van Donkelaar, A., Martin, R. V., Brauer, M., Kahn, R., Levy, R., Verduzco, C., and Villeneuve, P. J., 2010, "Global Estimates of Ambient Fine Particulate Matter Concentrations from Satellite-Based Aerosol Optical Depth: Development and Application," *Environ. Health Perspect.*, **118**(6), pp. 847–855.

[8] Whitaker, S. M., Peterson, B., Miller, A. F., and Bons, J. P., 2016, "The Effect of Particle Loading, Size, and Temperature on Deposition in a Vane Leading Edge Impingement Cooling Geometry," GT2016-57413.

[9] Crosby, J. M., Lewis, S., Bons, J. P., Ai, W., and Fletcher, T. H., 2008, "Effects of Temperature and Particle Size on Deposition in Land Based Turbines," *J. Eng. Gas Turbines Power*, **130**(5), p. 051503.

[10] El-Batsh, H., 2001, "Modeling Particle Deposition on Compressor and Turbine Blade Surfaces," Vienna University of Technology.

[11] Singh, S., and Tafti, D., 2015, "Particle Deposition Model for Particulate Flows at High Temperatures in Gas Turbine Components," *Int. J. Heat Fluid Flow*, **52**, pp. 72–83.

[12] Sreedharan, S. S., and Tafti, D. K., 2010, "Composition Dependent Model for the Prediction of Syngas Ash Deposition With Application to a Leading Edge Turbine Vane," GT2010-23655.

[13] Hsu, K., Barker, B., Varney, B., Boulanger, A., Nguyen, V., and Ng, W. F., 2018, "Review

of Heated Sand Particle Deposition Models," GT2018-75723.

[14] Ai, W., Murray, N., Fletcher, T. H., Harding, S., Lewis, S., and Bons, J. P., 2012, "Deposition Near Film Cooling Holes on a High Pressure Turbine Vane," *J. Turbomach.*, **134**(4), p. 041013.

[15] Lawson, S. A., Thole, K. A., Okita, Y., and Nakamata, C., 2012, "Simulations of Multiphase Particle Deposition on a Showerhead With Staggered Film-Cooling Holes," *J. Turbomach.*, **134**(5), p. 051041.

[16] Sundaram, N., Barringer, M. D., and Thole, K. A., 2008, "Effects of Deposits on Film Cooling of a Vane Endwall Along the Pressure Side," *J. Turbomach.*, **130**(4), p. 041006.

[17] Borello, D., D'Angeli, L., Salvagni, A., Venturini, P., and Rispoli, F., 2014, "Study of Particles Deposition in Gas Turbine Blades in Presence of Film Cooling," GT2014-26250.

[18] Kim, J., Dunn, M. G., Baran, A. J., Wade, D. P., and Tremba, E. L., 1993, "Deposition of Volcanic Materials in the Hot Sections of Two Gas Turbine Engines," *J. Eng. Gas Turbines Power*, **115**(3), p. 641.

[19] Lewis, S., Barker, B., Bons, J. P., Ai, W., and Fletcher, T. H., 2011, "Film Cooling Effectiveness and Heat Transfer Near Deposit-Laden Film Holes," *J. Turbomach.*, **133**(3), p. 031003.

[20] Prenter, R., Ameri, A., and Bons, J. P., 2016, "Deposition on a Cooled Nozzle Guide Vane With Nonuniform Inlet Temperatures," *J. Turbomach.*, **138**(10), p. 101005.

[21] Ogiriki, E. A., Yiguang, G. L., Theoklis, N., ThankGod, E. I., and Gowon, S., 2015, "Effect of Fouling, Thermal Barrier Coating Degradation and Film Cooling Holes Blockage on Gas Turbine Engine Creep Life," The Fourth International Conference on Through-Life Engineering Services, pp. 228–233.

[22] Cardwell, N. D., Sundaram, N., and Thole, K. A., "Effect of Midpassage Gap, Endwall Misalignment, and Roughness on Endwall Film-Cooling," *J. Turbomach.*, **128**(1), pp. 62–70.

[23] Mensch, A., and Thole, K., 2015, "Simulations of Multiphase Particle Deposition on a Gas Turbine Endwall With Impingement and Film Cooling," *J. Turbomach.*, **137**(11), p. 111002.

[24] Dunn, M. G., Padova, C., and Adams, M., 1987, *Operation of Gas Turbine Engines in Dust-Laden Environments*.

[25] Shah, A., and Tafti, D. K., 2007, "Transport of Particulates in an Internal Cooling Ribbed Duct," *J. Turbomach.*, **129**(4), pp. 816–825.

[26] Walsh, W. S., Thole, K. A., and Joe Pratt, C., 2006, "Effects of Sand Ingestion on the

Blockage of Film-Cooling Holes," GT2006-90067.

[27] Cardwell, N. D., Thole, K. A., and Burd, S. W., 2010, "Investigation of Sand Blocking Within Impingement and Film-Cooling Holes," *J. Turbomach.*, **132**(2), p. 021020.

[28] Jensen, J. W., Squire, S. W., Bons, J. P., and Fletcher, T. H., 2005, "Simulated Land-Based Turbine Deposits Generated in an Accelerated Deposition Facility," *J. Turbomach.*, **127**(3), pp. 462–470.

[29] AFRL-05 Data Sheet, 2017.

[30] NextEngine, 2016, "3D Laser Scanner."

[31] Kline, S. J., and McClintock, F. A., 1953, "Describing the Uncertainties in Single Sample Experiments," *Mech. Eng.*, **75**(1953), pp. 3–8.

[32] Barringer, M. D., Thole, K. A., Breneman, D. L., Tham, K. M., and Laurello, V., 2013, "Effects of Centrifugal Forces on Particle Deposition for a Representative Seal Pin between Two Blades," *J. Eng. Gas Turbines Power*, **135**, p. 032601.

[33] Lundgreen, R. K., 2017, "Pressure and Temperature Effects on Particle Deposition in an Impinging Flow," GT2017-64649.

[34] Yin, X. W., Cheng, L. F., Zhang, L. T., Travitzky, N., and Greil, P., 2017, "Fibre-Reinforced Multifunctional SiC Matrix Composite Materials," *Int. Mater. Rev.*, **62**(3), pp. 117–172.

[35] Chawla, K. K., 1998, "Chapter 7: Ceramic Matrix Composites," *Composite Materials*, Springer, Berlin, pp. 212–251.

[36] Ohnabe, H., Masaki, S., Onozuka, M., Miyahara, K., and Sasa, T., 1999, "Potential Application of Ceramic Matrix Composites to Aero-Engine Components," *Compos. Part A Appl. Sci. Manuf.*, **30**(4), pp. 489–496.

[37] Walock, M. J., Heng, V., Nieto, A., Ghoshal, A., Murugan, M., and Driemeyer, D., 2018, "Ceramic Matrix Composite Materials for Engine Exhaust Systems on Next-Generation Vertical Lift Vehicles," *J. Eng. Gas Turbines Power*, **140**(10), pp. 1–14.

[38] Tong, M. T., 2010, "An Assessment of the Impact of Emerging High-Temperature Materials on Engine Cycle Performance," GT2010-22361.

[39] Zhu, D., 2018, "Aerospace Ceramic Materials: Thermal, Environmental Barrier Coatings and SiC/SiC Ceramic Matrix Composites For Turbine Engine Applications," *NASA/TM—2018-219884*.

[40] Alvin, M. A., Bhatt, R., Grady, J., Warnes, B., Anderson, I., Heidloff, A., White, E., and McMordie, B., 2015, "Development of Advanced Material Systems for Future Gas Turbine Applications," GT2015-43456.

[41] Presby, M. J., Nesredin, K., Sanchez, L. J., Faucett, D. C., Choi, S. R., and Morscher, G. N., 2019, “Life-Limiting Behavior of an Oxide/Oxide Ceramic Matrix Composite at Elevated Temperature Subject to Foreign Object Damage,” *J. Eng. Gas Turbines Power*, **141**(3), pp. 1–7.

[42] Dassios, K. G., Aggelis, D. G., Kordatos, E. Z., and Matikas, T. E., 2013, “Cyclic Loading of a SiC-Fiber Reinforced Ceramic Matrix Composite Reveals Damage Mechanisms and Thermal Residual Stress State,” *Compos. Part A Appl. Sci. Manuf.*, **44**, pp. 105–113.

[43] Watanabe, F., Nakamura, T., and Mizokami, Y., 2017, “Design and Testing for Ceramic Matrix Composite Turbine Vane,” GT2017-63264.

[44] Watanabe, F., Nakamura, T., and Shinohara, K. I., 2016, “The Application of Ceramic Matrix Composite to Low Pressure Turbine Blade,” GT2016-56614.

[45] Krishna, K., Ricklick, M., Poinsatte, P., and Thurman, D., 2016, “Preliminary Investigation of an Oblique Jet Impingement Cooling on CMC Rough Surface,” 52nd AIAA/SAE/ASEE Joint Propulsion Conference, AIAA 2016-4851.

[46] Krishna, K., and Ricklick, M., 2017, “Heat Transfer Analysis of Jet Impingement Cooling on a Simulated Ceramic Matrix Composite Surface,” GT2017-64991.

[47] Wilkins, P. H., Lynch, S. P., Thole, K. A., Quach, S., and Vincent, T., 2020, “Experimental Heat Transfer and Boundary Layer Measurements on a Ceramic Matrix Composite Surface,” GT2020-15053.

[48] Nemeth, N. N., Mital, S. K., and Lang, J., 2010, “Evaluation of Solid Modeling Software for Finite Element Analysis of Woven Ceramic Matrix Composites,” *NASA/TM 2010-216250*.

[49] TexGen (2007), Version 3.11.0, User’s Guide.

[50] Stimpson, C. K., Snyder, J. C., Thole, K. A., and Mongillo, D., 2016, “Roughness Effects on Flow and Heat Transfer for Additively Manufactured Channels,” *J. Turbomach.*, **138**(5), pp. 1–10.

[51] Snyder, J. C., Stimpson, C. K., Thole, K. A., and Mongillo, D., 2016, “Build Direction Effects on Additively Manufactured Channels,” *J. Turbomach.*, **138**(5), pp. 1–8.

[52] Figliola, R. S., and Beasley, D. E., 1995, “Theory and Design for Mechanical Measurements, Second Edition,” *Eur. J. Eng. Educ.*, **20**(3), pp. 386–387.

[53] STARCCM+, Version 14.04.011, Product Overview.

[54] Colebrook, C. F., Blench, T., Chatley, H., Essex, E. H., Finnicome, J. R., Lacey, G., Williamson, J., and Macdonald, G. G., 1939, “Correspondence. Turbulent Flow in Pipes,

With Particular Reference To the Transition Region Between the Smooth and Rough Pipe Laws," *J. Inst. Civ. Eng.*, **12**(8), pp. 393–422.

[55] Gnielinski, V., 1976, "New Equations for Heat and Mass Transfer in Turbulent Pipe and Channel Flow," *Int. Chem. Eng.*, **16**(2), pp. 359–368.

[56] Park, J. S., Han, J. C., Huang, Y., Ou, S., and Boyle, R. J., 1992, "Heat Transfer Performance Comparisons of Five Different Rectangular Channels with Parallel Angled Ribs," *Int. J. Heat Mass Transf.*, **35**(11), pp. 2891–2903.